The Journal of Chemical Physics

RESEARCH ARTICLE | JULY 16 2025

Gravitational effect on the equilibrium contact angles of sessile droplets: Theory and simulations

Franziska Aurbach ; Fei Wang ; Britta Nestler

J. Chem. Phys. 163, 034706 (2025)
https://doi.org/10.1063/5.0275605

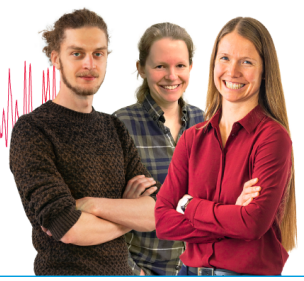

The Journal of Chemical Physics ARTICLE pubs.aip.org/aip/jcp

Gravitational effect on the equilibrium contact angles of sessile droplets: Theory and simulations

Cite as: J. Chem. Phys. 163, 034706 (2025); doi: 10.1063/5.0275605
Submitted: 14 April 2025 • Accepted: 24 June 2025 •
Published Online: 16 July 2025

Franziska Aurbach,[1,2] Fei Wang,[1,2,a)] and Britta Nestler[1,2,3]

AFFILIATIONS

[1] Institute of Applied Materials-Microstructure Modelling and Simulation, Karlsruhe Institute of Technology, Straße am Forum 7, 76131 Karlsruhe, Germany
[2] Institute of Nanotechnology, Karlsruhe Institute of Technology, Hermann-von-Helmholtz-Platz 1, 76344 Eggenstein-Leopoldshafen, Germany
[3] Institute of Digital Materials Science, Karlsruhe University of Applied Sciences, Moltkestraße 30, 76133 Karlsruhe, Germany

[a)] **Author to whom correspondence should be addressed:** fei.wang@kit.edu

ABSTRACT

This study extends the investigation of the wetting phenomenon to larger droplets on a smooth solid substrate, where gravitational effects become significant. We examine three distinct droplet geometries: a spherical cap, an oblate spheroidal cap, and a pancake shape, and we observe that the approximated droplet shape depends on the droplet size and the interfacial tensions. For small droplets on a smooth solid substrate, the droplet shape is assumed to be a spherical cap. However, as the droplet size increases, the equilibrium shape of the droplet becomes deformed due to the effect of gravity. The actual equilibrium contact angles, here referred to as microscopic contact angles, are determined by Young's law and are independent of droplet size or axisymmetric shape. Macroscopic contact angles are obtained by approximating the droplet shape with a geometric model and minimizing the free energy without assuming the validity of Young's law. We extend this concept to larger droplets and systematically compare these macroscopic angles with the microscopic ones. Our results demonstrate a correlation between the macroscopic contact angle and droplet size, with significant deviations from Young's law, increasing with droplet size. These findings are consistent with the Allen–Cahn model. Furthermore, we highlight the impact of the chosen measurement method on the accuracy of the contact angle, which varies with droplet size. In addition, the contact angle hysteresis—caused by varying liquid–solid and solid–gas interfacial tensions, which describes an intermolecular rearrangement of the liquid and gas species in an adsorption layer on the microscopic scale—is also influenced by the droplet size.

I. INTRODUCTION

Figure 1(a)(i) illustrates a droplet deposited on a smooth solid substrate in a gas phase, such as air, forming an apparent contact angle. The liquid, gas, and solid phases are denoted by L, G, and S, respectively. The interfacial tensions of liquid–gas, liquid–solid, and solid–gas are represented by σ, γ_L, and γ_G, respectively. This phenomenon, known as the wetting effect, manifests in various everyday applications, such as self-cleaning surfaces and inkjet printing,[1] and is also observed for larger droplets in liquid lenses.[2] It is influenced by several physical factors, including surface roughness and heterogeneity.[3]

For small droplets, the effect of body energy is negligible, and the droplet shape can be approximated as a spherical cap with volume V and cap radius R, illustrated in Fig. 2,

$$V = \frac{\pi R^3}{3}(1-\cos\theta)^2(2+\cos\theta), \tag{1}$$

$$R = \left[\frac{3V}{\pi(1-\cos\theta)^2(2+\cos\theta)}\right]^{\frac{1}{3}}. \tag{2}$$

The surface area of the liquid–gas interface is given by

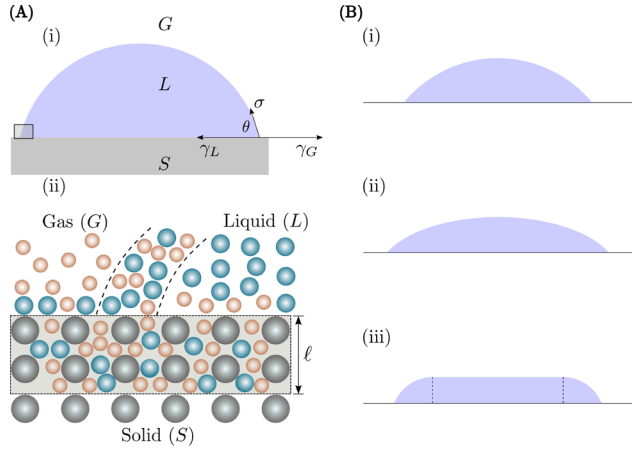

FIG. 1. (a)(i) Schematic cross-sectional view of the liquid droplet (*L*, blue) on a solid substrate (*S*, gray) in a gas phase (*G*, white), showing the contact angle θ and the interfacial tensions σ, γ_G, and γ_L, and (ii) sketch of the surface composition, illustrating a liquid droplet (*L*, blue) on a solid substrate (*S*, gray) in a gas phase (*G*, orange), with intermolecular rearrangements at the adsorption layer. (b) Cross-sectional view of the three considered shapes of the liquid droplet: (i) spherical cap, (ii) oblate spheroidal cap, and (iii) pancake shape.

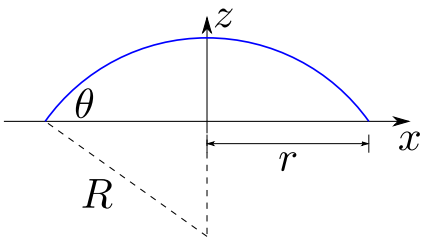

FIG. 2. Illustration of the cap radius R and the base radius $r = R\sin\theta$ of the liquid droplet formed by a spherical cap.

$$S_{LG} = 2\pi R^2(1-\cos\theta).$$

The total surface energy of the system can be expressed as

$$E_I = \sigma S_{LG} + \gamma_L \pi (R\sin\theta)^2 + \gamma_G[S - \pi(R\sin\theta)^2], \tag{3}$$

where S represents the total area of the solid surface. It consists of the liquid–gas, liquid–solid, and solid–gas interfacial energies, respectively. By incorporating the volume constraint from Eq. (2) and defining $\Delta\gamma = \gamma_G - \gamma_L$, the total surface energy in Eq. (3) can be rewritten as

$$E_I = \left[\frac{9\pi V^2}{(1-\cos\theta)(2+\cos\theta)^2}\right]^{\frac{1}{3}}[2\sigma - \Delta\gamma(1+\cos\theta)] + \gamma_G S.$$

The derivative of E_I with respect to θ is given by

$$\frac{dE_I}{d\theta} = \left[\frac{9V^2\pi}{(1-\cos\theta)^4(2+\cos\theta)^5}\right]^{\frac{1}{3}} 2(\Delta\gamma - \sigma\cos\theta)\sin\theta.$$

Setting $dE_I/d\theta = 0$ and solving for θ, we obtain the equilibrium contact angle, which satisfies Young's law,[4]

$$\cos\theta_{YL} = \frac{\gamma_G - \gamma_L}{\sigma}. \tag{4}$$

This equation is based on several simplified assumptions and, for example, does not account for surface roughness or heterogeneity. Since measuring the interfacial tensions γ_G and γ_L individually is challenging, their difference $\Delta\gamma := \gamma_G - \gamma_L$ is typically determined through contact angle measurements.

In the analysis above, gravitational effects were neglected, as the calculations were restricted to small droplets.

In the following, we incorporate gravitational effects and distinguish between two concepts of equilibrium contact angles: microscopic and macroscopic contact angles. We define microscopic contact angles by the actual equilibrium contact angles at the three-phase contact line. For axisymmetric droplets, it can be derived by applying the transversality condition[5,6] or, alternatively, by calculating the droplet profile that minimizes $F - pV$, where F represents the free energy and the Lagrange multiplier p enforces volume conservation.[7] Both methods yield Young's law, which is independent of the droplet size and unaffected by gravity. Macroscopic contact angles are obtained by minimizing the total free energy using an approximated droplet geometry. As larger droplets become increasingly deformed and flattened compared to a spherical cap due to gravity, the approximated geometry depends on the droplet size. To account for this, we employ three geometric models for approximating the droplet shape, whose cross-sectional profiles are shown in Fig. 1(b): the spherical cap, the oblate spheroidal cap, and the pancake shape. Previous studies have primarily focused on small droplets that can be well described by an oblate spheroidal cap.[8] This study extends the approach to larger droplets, systematically comparing the macroscopic contact angles obtained with the respective microscopic ones. It illustrates the influence of the droplet size and the choice of contact angle measurement method on the accuracy of contact angles.

The total free energy is determined as the sum of the interfacial energies E_S, which is analogous to the previously described case of the spherical cap, and the body energy E_G.

In Ref. 9, the droplet shapes are considered as a spherical cap, an oblate spheroidal cap, and a pancake shape. Here, Young's law is used to describe the equilibrium contact angle for each shape, with the pancake shape simplified by omitting the rounded edge. Furthermore, the effect of line tension on the equilibrium contact angle was examined in Refs. 9 and 10. In addition, the intermolecular rearrangements of liquid and gas species in the adsorption layer were included, as in Ref. 11. By applying the transversality condition, Young's contact angle is independent of the gravitational effect.[5–7] The gravitational effect on the oblate spheroidal cap droplet model is addressed in Refs. 8 and 12, which includes the calculation of the equilibrium contact angle by energy minimization, differing from Young's law. In Ref. 13, the RTEA (surface of revolution by rotating two elliptic arcs) model is developed to describe the shape of heavy droplets on hydrophobic surfaces since the symmetry of the oblate spheroidal model is inconsistent with the Young–Laplace equation. In Ref. 14, a size-dependent term in Young's equation, resulting from gravity, is examined.

In the literature,[8,9] the pancake shape was assumed to be a cylinder, the rounded edges were neglected, and the equilibrium contact angle for this droplet model has not been investigated previously.

The remaining manuscript is structured as follows: first, we present the Blokhuis–Shilkrot–Widom derivation of the microscopic contact angle in the presence of gravity in Sec. II. We present a theoretical investigation of energy minimization and the macroscopic contact angles of the droplet shaped as an oblate spheroidal cap in Sec. III A and a pancake shape in Sec. III B. Subsequently, these geometries are compared to determine which shape provides the most accurate approximation in Sec. III C, depending on the droplet size and $\Delta\gamma/\sigma$. In Sec. IV, we present and compare energy landscapes by varying the liquid–gas and solid–liquid interfacial tensions as functions of surface compositions for different values of S/R_0^2 and for the three considered droplet shapes. This analysis aims to elucidate the differences in contact angle hysteresis on a smooth solid substrate, induced by molecular rearrangements in an adsorption layer, as illustrated in Fig. 1(a)(ii), across various droplet sizes. In addition, we provide macroscopic contact angle maps for each geometrical droplet shape model, along with maps of the geometrical parameters of both the oblate spheroidal cap and the pancake shape. In addition, we present the results of the Allen–Cahn model[15] in Sec. V, where the contact angles are measured using two different methods and compared with the theoretical predictions. This is followed by a conclusion in Sec. VI and an outlook in Sec. VII.

II. MICROSCOPIC CONTACT ANGLE: THE CLASSIC DERIVATION OF YOUNG'S LAW WITH GRAVITY

In Refs. 7, 16, and 17, the droplet profile $\eta(z)$ and the contact angle, which minimize the free energy F, are calculated. The first term of the free energy represents the gravitational energy, with the gravitational acceleration g and the density difference between the liquid and gas phases $\Delta\rho$. This term is added to the second and third terms, which describe the interfacial energies, similar to those described in Sec. I,

$$F = \int \Delta\rho g z \mathrm{d}V + \int \sigma \mathrm{d}S_{LG} - \int \Delta\gamma \mathrm{d}S_{SL},$$

where S_{LG} and S_{SL} represent the liquid–gas and solid–liquid interfacial areas, respectively. The profile $\eta(z)$, sketched in Fig. 3, represents the radius of the droplet shape at a given height z with respect to the solid surface. The droplet is considered to be rotationally symmetric with respect to the z-axis, and the free energy functional is, thus, given by

$$F[\eta] = \int_0^h \Delta\rho g z \pi \eta(z)^2 + \sigma 2\pi\eta(z)\left[1+\eta'(z)^2\right]^{\frac{1}{2}} - \Delta\gamma\pi\eta(z)^2\delta(z)\mathrm{d}z,$$

where h denotes the height of the droplet and δ is the Dirac delta function. In order to fix the droplet volume, the Lagrange multiplier p is introduced, and the following term is added:

$$-p\int \mathrm{d}V = -p\int_0^h \pi\eta(z)^2\mathrm{d}z.$$

Since the aim is to find the shape $\eta(z)$ that minimizes the free energy, the functional derivative $\frac{\delta[F-pV]}{\delta\eta(z')}$ is considered, given by

$$\frac{\delta[F-pV]}{\delta\eta(z')} = \int_0^h \left\{(-p+\Delta\rho g z)2\pi\eta(z) + \frac{\sigma 2\pi}{\left[1+\eta'(z)^2\right]^{\frac{1}{2}}} - \sigma\frac{2\pi\eta(z)\eta''(z)}{\left[1+\eta'(z)^2\right]^{\frac{3}{2}}} - \Delta\gamma 2\pi\eta(z)\delta(z)\right\}\delta(z-z')\mathrm{d}z + \left[\sigma 2\pi\eta(z)\frac{\eta'(z)}{\left[1+\eta'(z)^2\right]^{\frac{1}{2}}}\delta(z-z')\right]_{z=0}^{z=h}. \quad (5)$$

The boundary term in Eq. (5) emerges through integration by parts. The minimization of the free energy $\frac{\delta[F-pV]}{\delta\eta(z')}$ leads to the Laplace equation and a boundary term, namely, Young's equation equivalent to Eq. (4), which defines the microscopic contact angle and remains unaffected by gravity.[7]

III. MACROSCOPIC CONTACT ANGLE: APPROXIMATION BY A GEOMETRIC MODEL

In this section, we consider a liquid droplet of arbitrary size in the gas phase on a solid substrate. The droplet size is related to the Bond number $\mathrm{Bo} = \Delta\rho R_0^2 g/\sigma$, where g denotes the gravitational acceleration and $\Delta\rho = \rho_L - \rho_G$ represents the density difference between the liquid and gas phases. The initial radius, R_0, defines the radius of a spherical droplet before it is placed on the surface, with the volume given by $V = \frac{4}{3}\pi R_0^3$. We focus on three geometric models for the droplet shape: the spherical cap, the oblate spheroidal cap, and the pancake shape.

The body energy of the droplet can be expressed as

$$E_G = \Delta\rho g \bar{z} V,$$

where $\bar{z}$ represents the height of the droplet's centroid relative to the solid substrate.

The free surface energy is given by the sum of the interfacial energies of the liquid–gas, solid–liquid, and solid–gas interfaces,

$$E_S = \sigma S_{LG} + \gamma_L S_{SL} + \gamma_G S_{SG}. \quad (6)$$

The surface areas of the liquid–gas, solid–liquid, and solid–gas interfaces are represented by S_{LG}, S_{SL}, and S_{SG}, respectively. The total area of the solid surface is represented as $S = S_{SL} + S_{SG}$ and the interfacial tensions of the liquid–gas, solid–liquid, and solid–gas are given by σ,

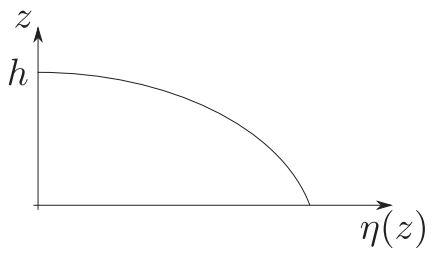

FIG. 3. Half contour line of the droplet, characterized by $\eta(z)$.

γ_L, and γ_G, respectively. We obtain the total energy by summing the surface energy and the body energy as

$$E = E_S + E_G = \sigma S_{LG} - \Delta\gamma S_{SL} + \gamma_G S + \Delta\rho g \bar{z} V, \tag{7}$$

where $\Delta\gamma = \gamma_G - \gamma_L$. Based on the preceding theoretical framework, the macroscopic contact angle is obtained by minimizing the total free energy.

A. Energy minimization of the oblate spheroidal cap model

The blue line in Fig. 4 represents a droplet shaped as an oblate spheroidal cap, which will be investigated in the following. It is formed by an oblate spheroid, whose contour can be described by rotating an ellipse, as defined by the parametric equation,

$$\alpha^3 x^2 + (z - \alpha R)^2 = \alpha^2 R^2,$$

with $0 < \alpha \leq 1$ around the z-axis. The oblate spheroid is truncated such that the contact angle θ is formed on the solid surface. The vertical semi-minor axis of the oblate spheroid is $R\alpha$, while the horizontal semi-major axis is $R/\sqrt{\alpha}$. The red dashed line in Fig. 4 depicts an imaginary spherical cap with an equivalent volume to the oblate spheroidal cap and the contact angle θ_c. This spherical cap is used to calculate the liquid–gas interface surface area, derived in Appendix A, and the solid–liquid interface surface area,

$$S_{LG} = \omega\left(\alpha^3\left(\operatorname{arcsinh}\left(\frac{\psi\phi}{\alpha^{\frac{3}{2}}}\right) - \operatorname{arcsinh}\left(\frac{\psi}{\alpha^{\frac{3}{2}}}\right)\right) + \nu - \psi\right), \tag{8}$$

$$S_{SL} = \frac{\pi R^2 \sin^2\theta_c}{\alpha}, \tag{9}$$

with

$$\nu = \phi\sqrt{-\left(\cos^2(\theta_c)\right)\alpha^3 + \alpha^3 + \cos^2(\theta_c)}\psi,$$

$\psi = \sqrt{1-\alpha^3}$, $\phi = \cos\theta_c$, and $\omega = -\frac{R^2\pi}{\psi\alpha}$. The derivation of the volume and the height of the centroid of the oblate spheroidal cap can be found in Appendixes B and C, respectively,

$$V = \frac{\pi}{3}R^3(1-\cos\theta_c)^2(2+\cos\theta_c), \tag{10}$$

$$V\bar{z} = \frac{\alpha\pi R^4}{12}(1-\cos\theta_c)^3(3+\cos\theta_c). \tag{11}$$

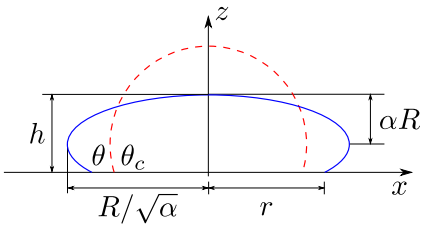

FIG. 4. Schematic sectional view of the droplet represented as an oblate spheroidal cap (blue line) with the macroscopic contact angle θ and the imaginary spherical cap (red dashed line) having the same volume as the oblate spheroidal cap and the corresponding imaginary contact angle θ_c.

By applying the volume constraint Eq. (10), the previous equations, namely, Eqs. (7), (8), (9), and (11), the free energy can be expressed as a function $E_{II}(\theta_c, \alpha)$. The macroscopic contact angle θ can be calculated by the imaginary contact angle θ_c and the parameter α, as detailed in Appendix D, being consistent with Ref. 8,

$$\theta = \begin{cases} \arctan\left(\alpha^{\frac{3}{2}}\tan\theta_c\right) & 0 < \theta_c < \frac{\pi}{2}, \\ \frac{\pi}{2} & \theta_c = \frac{\pi}{2}, \\ \arctan\left(\alpha^{\frac{3}{2}}\tan\theta_c\right) + \pi & \frac{\pi}{2} < \theta_c < \pi. \end{cases}$$

The equilibrium oblate spheroidal cap is obtained by using the parameters α and θ_c to minimize the energy $E_{II}(\theta_c, \alpha)$ over the domain $\Omega := \{(\alpha, \theta_c) | 0 < \alpha \leq 1, 0 < \theta_c < \pi\}$. Consequently, we solve the equations $\partial E_{II}/\partial\alpha = 0$ and $\partial E_{II}/\partial\theta_c = 0$. This system of equations is generally not analytically solvable and is solved numerically. An exemplary energy landscape for $E_{II}(\theta_c, \alpha)$ on Ω is shown in Fig. 5, where the unique energy minimum in Ω is marked by a cross.

Figure 6(a) shows the macroscopic contact angle θ, obtained through energy minimization of $E_{II}(\theta_c, \alpha)$, for different Bond numbers, as a function of $\Delta\gamma/\sigma$. This behavior is consistent with the findings in Ref. 12. It can be observed that the macroscopic contact angle of the oblate spheroidal model depends on the Bond number, and thus on the droplet size, the density difference $\Delta\rho$, the gravitational acceleration g, and the interfacial tensions between the liquid–solid, solid–gas, and liquid–gas phases. These interfacial tensions also influence Young's law. In general, these curves are not centrally symmetric with respect to $(\Delta\gamma/\sigma, \theta) = (0, 90^\circ)$, in contrast to Young's law. They do not pass through the point $(\Delta\gamma/\sigma, \theta) = (0, 90^\circ)$, which implies that the rule derived from Young's law, stating $\Delta\gamma \geq 0$ for hydrophilic wetting and $\Delta\gamma < 0$ for hydrophobic wetting, does not hold in this case.

In addition, Young's law matches the macroscopic contact angle θ obtained by energy minimization of the surface energy, as given by Eq. (6), excluding the body energy. The contact angle converges to Young's law with decreasing Bond number or droplet size, respectively. For superhydrophobic contact angles, a significant deviation (of 28° for Bo = 1) can be observed. For small Bond numbers (Bo ≤ 1), the deviation between the macroscopic contact

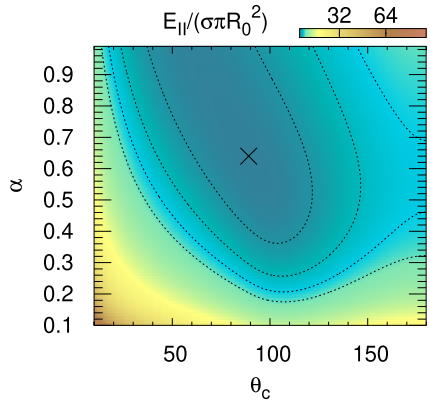

FIG. 5. Energy landscape $E_{II}(\theta_c, \alpha)$ of the oblate spheroidal cap for $\Delta\gamma/\sigma = 0.0625$, with the unique energy minimum marked by a cross.

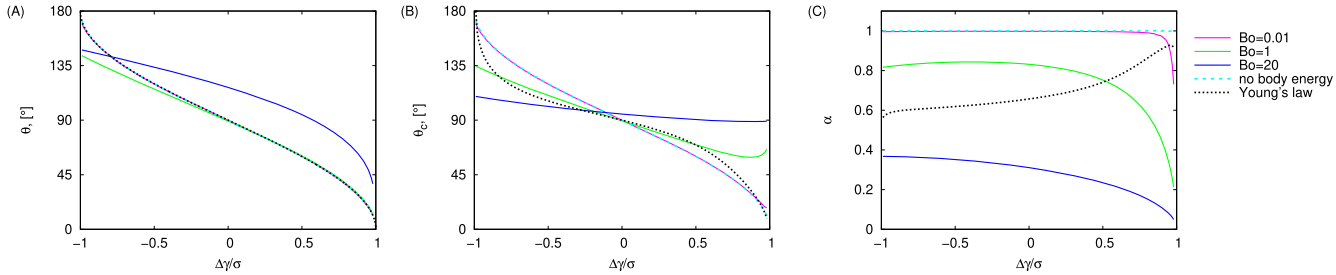

FIG. 6. (a) Macroscopic contact angle θ, (b) imaginary contact angle θ_c, and (c) parameter α of the oblate spheroidal cap by energy minimization as a function of $\Delta\gamma/\sigma$ for different Bond numbers: Bo = 0.01 (pink), Bo = 1 (green), and Bo = 20 (blue) compared to the curves neglecting body energy (cyan dashed line) and Young's law (black dashed line).

angle and Young's law decreases as $\Delta\gamma/\sigma$ decreases and shows a good agreement.

In Fig. 6(b), the corresponding imaginary contact angles θ_c are presented. As the Bond number decreases, the imaginary contact angles, θ_c, approach those determined by energy minimization while neglecting the body energy (cyan dashed line).

The dependence of the equilibrium parameter α on $\Delta\gamma/\sigma$ is shown in Fig. 6(c). The black dashed line, derived from Young's law, does not coincide with the cyan dashed line obtained by minimizing the surface energy of the oblate spheroidal cap model, Eq. (6), while neglecting the body energy. It follows a qualitatively different course compared to the other curves. The solid lines, representing the parameter α obtained through energy minimization of the oblate spheroidal cap model, approach α obtained by minimizing the surface energy and neglecting the body energy (cyan dashed line) as the Bond number decreases. These solid lines converge to 0 as $\Delta\gamma/\sigma$ approaches 1.

The agreement of the equilibrium contact angles of the oblate spheroidal cap model from Young's law indicates the validity of this model.[12]

B. Energy minimization of the pancake shape model

The pancake shape model, which is investigated in the following, is shown in Fig. 7. It consists of a flat cylindrical part with the radius r_1 and the height h at the center and a rounded edge, which can be regarded as part of a torus with major radius r_1 and minor radius R. The pancake is shaped in such a way that the contact angle θ is formed. Rigorously speaking, the flat cylindrical part does not occur in a physical droplet. The pancake shape model is employed to approximate the droplet profile for large droplets, where the height remains nearly constant near the center. The surface area of the liquid–gas interface S_{LG}, the volume V, and the height of the centroid $\bar{z}$ are calculated in Appendixes E–G, respectively,

$$S_{LG} = \pi r_1^2 + 2\pi r_1 R\theta + 2\pi R^2(1-\cos\theta),$$
$$V = V_1 + V_2 - V_3,$$

with

$$V_1 = \pi r_1^2 R(1-\cos\theta),$$
$$V_2 = \pi R^2 r_1\theta + \frac{2\pi}{3}R^3(1-\cos\theta),$$
$$V_3 = \pi r\frac{\cos\theta}{\sin\theta}\left(\frac{1}{3}r^2 - r_1^2 + \frac{2r_1^3}{3r}\right),$$
$$V\bar{z} = \int_{V_1} z\mathrm{d}V_1 + \int_{V_2} z\mathrm{d}V_2 - \int_{V_3} z\mathrm{d}V_3,$$

with

$$\int_{V_1} z\mathrm{d}V_1 = \frac{\pi}{2}R^2(1-\cos\theta)^2 r_1^2,$$
$$\int_{V_2} z\mathrm{d}V_2 = 2\pi\left(\frac{R^3 r_1}{3}\lambda + \frac{R^4}{8}\lambda^2 + \frac{R^4}{3}\xi^2 - \frac{R^4}{3}\xi - \frac{R^3 r_1}{2}\xi\theta\right),$$
$$\int_{V_3} z\mathrm{d}V_3 = -\pi z_1^2\left(\frac{r^2}{12} - \frac{r_1^2}{2} + \frac{2r_1^3}{3r} - \frac{r_1^4}{4r^2}\right),$$
$$S_{SL} = \pi r^2,$$

with $r = r_1 + R\sin\theta$, $h = R(1-\cos\theta)$, $\xi = \cos\theta$, and $\lambda = \sin\theta$. By using the previous equations and eliminating the parameter r_1 through the volume constraint, the total free energy from Eq. (7) can, therefore, be considered a function $E_{III}(\theta, h)$ of the height h and the macroscopic contact angle θ. The equilibrium of the pancake shape can be numerically calculated by minimizing the energy $E_{III}(\theta, h)$ over the domain as

$$\Omega := \{(\theta, h) | 0 < \theta < \pi, 0 < h \le h_{\max}\}$$
$$h_{\max} = (1-\cos\theta)\left[\frac{3V}{\pi(1-\cos\theta)^2(2+\cos\theta)}\right]^{\frac{1}{3}},$$

where the maximum value $h_{\max}$ represents the height of a spherical cap with the contact angle θ and, therefore, $r_1 = 0$, as visualized in Fig. 8, and solving $\partial E_{III}(\theta, h)/\partial\theta = 0$ and $\partial E_{III}(\theta, h)/\partial h = 0$.

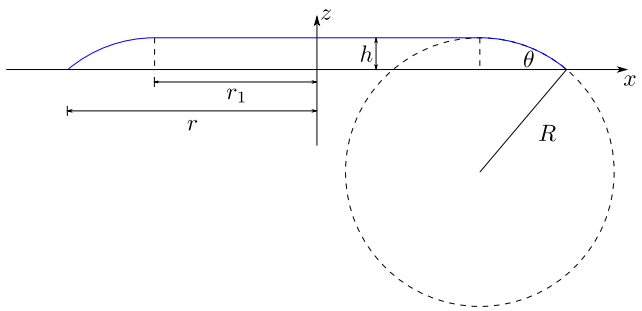

FIG. 7. Schematic sectional view of the droplet formed as a pancake.

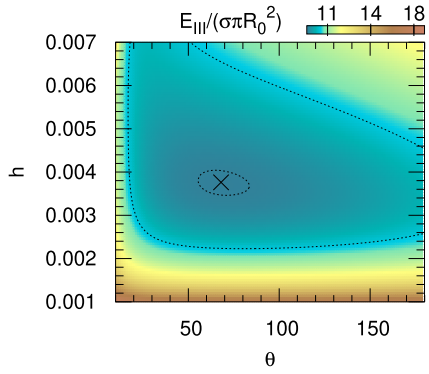

FIG. 8. Energy landscape $E_{III}(\theta, h)$ of the pancake shape for $\Delta\gamma/\sigma = 0.0625$, with the unique energy minimum marked by a cross.

Figure 9 shows the macroscopic contact angles θ obtained by energy minimization of $E_{III}(\theta, h)$ as a function of $\Delta\gamma/\sigma$ for different values of the Bond number, represented by colored solid lines, and Young's law as a black dashed line. We observe a dependence of the macroscopic contact angle on the Bond number, where the contact angle is decreasing with increasing Bond number. In addition, the contact angle depends on the liquid–gas, solid–liquid, and solid–gas interfacial tensions, which also influence Young's law, as well as the density difference $\Delta\rho$ and the gravitational acceleration.

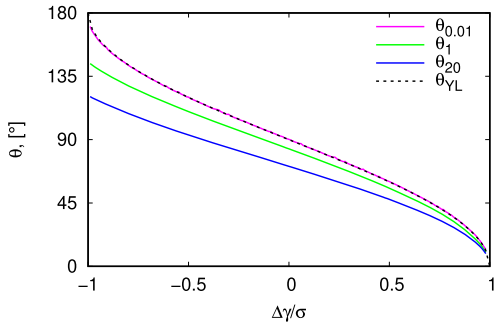

FIG. 9. Macroscopic contact angle θ of the pancake shape as a function of $\Delta\gamma/\sigma$ for different Bond numbers: $\theta_{0.01}$ with Bo = 0.01 (pink), θ_1 with Bo = 1 (green), and θ_{20} with Bo = 20 (blue), compared to Young's law θ_{YL} (black dashed line).

The macroscopic contact angles obtained through energy minimization converge to Young's law as the Bond number decreases. Therefore, the deviation of the droplet shape and the pancake shape is increasing with increasing Bond number. Furthermore, the deviation between the macroscopic contact angles obtained by energy minimization and Young's law decreases with increasing $\Delta\gamma/\sigma$. The observed curves do not intersect the point $(\Delta\gamma/\sigma, \theta) = (0, 90°)$, which suggests that the principle derived from Young's law—stating $\Delta\gamma \geq 0$ is applicable to hydrophilic wetting and $\Delta\gamma < 0$ pertains to hydrophobic wetting—is not applicable in the present scenario.

C. Comparison of the considered geometric droplet shape models

The capillary length $l = \sqrt{\sigma/(\Delta\rho g)}$ is defined by equating the Laplace pressure σ/l with the hydrostatic pressure $\Delta\rho g l$ and determines the initial drop radius R_0, which corresponds to Bo = 1. For small droplets ($R_0 \ll l$ or Bo $\ll$ 1), capillary forces dominate, and the curvature is constant, governed by the Laplace equation, resulting in a spherical cap. In contrast, for large droplets ($R_0 \gg l$ or Bo $\gg$ 1), gravitational forces prevail, leading to a flattened droplet shape.[18]

In Fig. 10(a), the energies of the spherical cap, including the gravitational energy (E_I), the oblate spheroidal cap (E_{II}), and the pancake shape (E_{III}), are shown as a function of the Bond number. It can be observed that the energy of the spherical cap approximates the energies of the oblate spheroidal cap and the pancake shape for small Bond numbers. For larger Bond numbers, the energy of the spherical cap exceeds the energy of the oblate spheroidal cap and the pancake shape, which are comparatively close to each other. The energy of the spherical cap is greater than or equal to the energy of both the oblate spheroidal cap and the pancake for all Bond numbers, as the spherical cap is a special case of the other shapes ($\alpha = 1$ and $r_1 = 0$, respectively), having one degree of freedom less,

$$E_I \geq E_{II} \text{ and } E_I \geq E_{III} \text{ for all Bo} > 0.$$

The difference in energy between the oblate spheroidal cap E_{II} and the pancake shape E_{III} near their intersection point is displayed in Fig. 10(b). Beyond this intersection point, at the Bond number Bo*, the energy difference $|E_{II} - E_{III}|/[\sigma^2\pi/(\Delta\rho g)]$ between the oblate spheroidal cap and the pancake shape increases monotonically, while before Bo*, it decreases. For negative values of

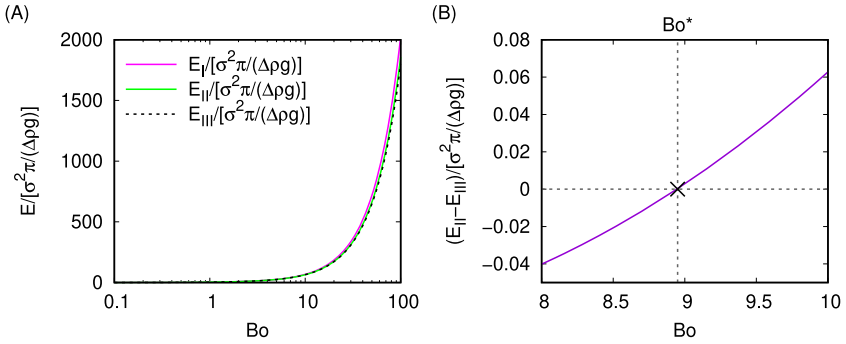

FIG. 10. (a) Energy of the spherical cap E_I (with gravity term) (pink), the oblate spheroidal cap E_{II} (green), and the pancake shape E_{III} (black dashed line) as a function of the Bond number for $\Delta\gamma/\sigma = 0.14$. (b) Difference between the energy of the oblate spheroidal cap E_{II} and the pancake shape E_{III} as a function of the Bond number, highlighting the intersection between the corresponding curves in (a).

$(E_{II} - E_{III})/[\sigma^2\pi/(\Delta\rho g)]$, the droplet shape is most accurately approximated by the oblate spheroidal cap, which corresponds to Bond numbers less than Bo*. Conversely, for positive values, the pancake shape model has a lower energy, occurring at Bond numbers larger than Bo*. Here, the geometric representation that most closely reproduces the droplet shape is the pancake shape model. The intersection of the curve with the horizontal axis, marked by the cross, yields the Bond number Bo* at which the energies of the oblate spheroidal cap and the pancake shape are equal,

$$E_{II} < E_{III} \text{ for Bo} < \text{Bo}^*,$$
$$E_{II} = E_{III} \text{ for Bo} = \text{Bo}^*,$$

and

$$E_{II} > E_{III} \text{ for Bo} > \text{Bo}^*.$$

The transition of the droplet shape from the oblate spheroidal cap to the pancake shape at Bo* is discontinuous, and consequently, a continuous transition is assumed in a neighborhood around Bo*.

Figure 11 shows the parameter α as a function of the Bond number for different values of $\Delta\gamma/\sigma$. As the Bond number decreases, α approaches 1, indicating that the droplet model is nearly spherical. In contrast, α converges to 0 for large Bond numbers, which corresponds to a flat and wide oblate spheroidal cap.

The parameters R and r_1 of the pancake, R of the oblate spheroidal cap, and R of the spherical cap are shown in Fig. 12(a). The radius R of the spherical cap, represented by the black line, and the parameter R of the oblate spheroidal cap increase monotonically with the Bond number, as the volume grows. For small Bond numbers, $r_1 \ll R$, and the pancake is approximately a spherical cap. For high Bond numbers, on the other hand, $r_1 \gg R$, and the pancake becomes flat and wide.

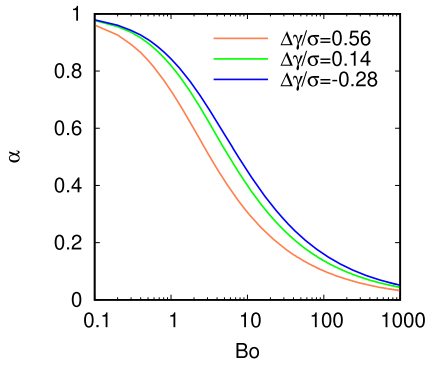

FIG. 11. Parameter α of the oblate spheroidal cap as a function of the Bond number for $\Delta\gamma/\sigma = 0.5625$ (orange), $\Delta\gamma/\sigma = 0.14$ (green), and $\Delta\gamma/\sigma = -0.28$ (blue).

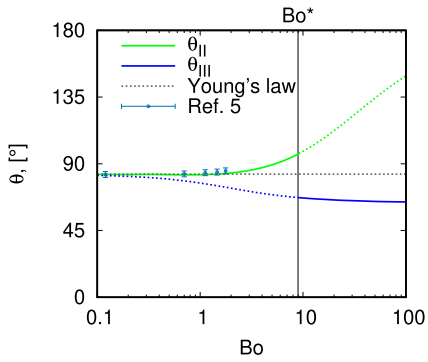

FIG. 13. Macroscopic contact angle of the oblate spheroidal cap θ_{II} (green) and the pancake shape θ_{III} (blue) as a function of the Bond number for $\Delta\gamma/\sigma = \arccos(83°)$ along with Young's law (gray dashed line), including the values from Ref. 8 with error bars due to measurement inaccuracies.

Overall, the droplet is approximately formed by a spherical cap for small Bond numbers, where $\alpha \approx 1$. For intermediate Bond numbers Bo < Bo*, the droplet is approximated with the highest accuracy by an oblate spheroidal cap, while it forms a pancake shape for large Bond numbers Bo > Bo*. Since the transition between the oblate spheroidal cap and the pancake shape is not continuous, a transition phase between the oblate spheroidal cap and the pancake shape around the transition Bond number Bo* is assumed.

Figure 13 shows the contact angle according to Young's law and the macroscopic contact angles of the oblate spheroidal cap θ_{II} and the pancake shape θ_{III} as a function of the Bond number. For small Bond numbers, the macroscopic contact angles of the oblate spheroidal cap and the pancake shape approach Young's law. The small deviations, within several degrees, of the macroscopic contact angles of the oblate spheroidal cap from Young's law for small Bond numbers (Bo < 1.77) are consistent with the values in Ref. 8 and the observations in Ref. 12. In addition, the experimental data in Ref. 19 show almost constant contact angles for small droplets (Bo < 4.5) on a smooth solid surface. The deviation between Young's law and the macroscopic contact angles of the oblate spheroidal cap and the pancake shape increases with increasing Bond number.

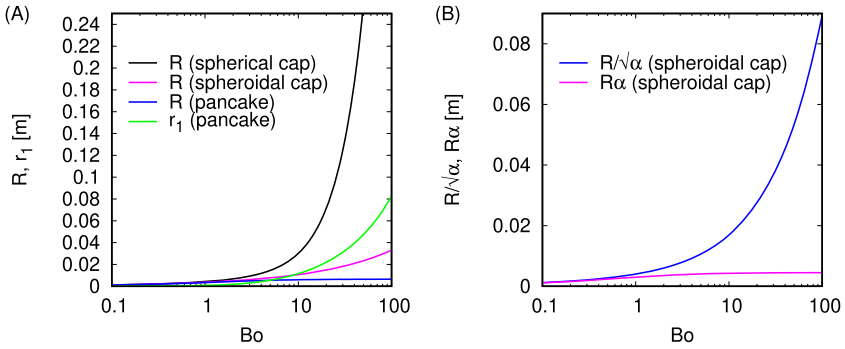

FIG. 12. (a) Parameter R of the spherical cap (including the gravitational energy) (black), R of the oblate spheroidal cap (pink), R of the pancake shape (blue), and r_1 of the pancake shape (green) with $\Delta\gamma/\sigma = 0.14$. (b) Horizontal semi-major axis $R/\sqrt{\alpha}$ (blue) and vertical semi-minor axis $R\alpha$ (pink) of the whole oblate spheroidal as a function of the Bond number with $\Delta\gamma/\sigma = 0.14$.

Notably, the macroscopic contact angle of the oblate spheroidal cap increases monotonically with increasing Bond number, while the macroscopic contact angle of the pancake shape decreases monotonically as the Bond number increases, which is attributed to an increase in hydrostatic pressure.[20] For large Bond numbers, there is a significant increase in the macroscopic contact angles of the oblate spheroidal cap (with a deviation of 66.97° at Bo = 100 from Young's law). In contrast, the macroscopic contact angles of the pancake shape show only a moderate deviation from Young's law (of 17.7° at Bo = 100). The large increase in the macroscopic contact angles of the oblate spheroidal cap, represented by the dashed green line, can be neglected because the droplet shape is best represented by the pancake shape for Bond numbers greater than Bo*. Therefore, the oblate spheroidal cap model does physically not occur in this case. At the transition Bond number Bo*, the transition between the macroscopic contact angle of the oblate spheroidal cap and the pancake shape, as well as the corresponding forms, is not continuous. It is assumed that there is a continuous transition between the oblate spheroidal cap and the pancake shape, which could be modeled by interpolation of both cases.

In Fig. 14(a), a decrease in the ratio of the droplet height to the initial drop radius of the oblate spheroidal cap h_{II}/R_0 and the pancake shape h_{III}/R_0 can be observed. However, an increase in the ratio of the base radius and the initial drop radius of the oblate spheroidal cap r_{II}/R_0 and the pancake shape h_{III}/R_0 is shown in Fig. 14(b). Both observations are consistent with the expected impact of the gravitational effect, which increases with the size of the droplets: the droplets become flatter and wider.

The Bond number Bo* at which the energies of the oblate spheroidal cap and the pancake intersect, marking the transition of the droplet shape from an oblate spheroidal cap to a pancake, is shown in Fig. 15 as a function of $\Delta\gamma/\sigma$. For a Bond number below the curve, the energy of the oblate spheroidal cap is lower, while for a Bond number above the curve, the energy of the pancake shape is lower. The transition Bond number between these two shapes decreases as $\Delta\gamma/\sigma$ increases. Thus, the oblate spheroidal cap provides the most accurate approximation of the droplet shape for much larger volumes in the superhydrophobic case, and a smaller droplet volume is required to form a geometry that resembles the pancake shape as $\Delta\gamma/\sigma$ increases and the surface becomes more hydrophilic. For superhydrophilic conditions, the pancake shape yields the best fit for much smaller droplets. The dependency of the droplet shape, whether approximated by a pancake or an oblate spheroidal cap on the contact angle (or the ratio $\Delta\gamma/\sigma$) was also studied in Ref. 21 for

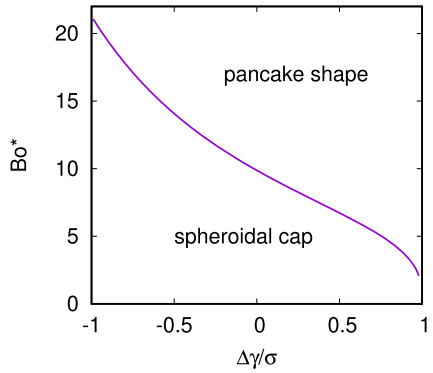

FIG. 15. Transition Bond number Bo*, at which the energies of the oblate spheroidal cap and pancake shape are equal, as a function of $\Delta\gamma/\sigma$. For a Bond number below the curve, a droplet formed by an oblate spheroidal cap has less energy than a droplet formed by a pancake shape, and for a Bond number above the curve, the droplet formed by a pancake shape has less energy than a droplet formed by an oblate spheroidal cap.

small contact angles and the limiting Bond number, at which the contact angle deviates from the contact angle of the spherical cap of 1°, was expressed as a function of the original contact angle.[22]

IV. CONTACT ANGLE HYSTERESIS CAUSED BY MICROSCOPIC ROUGHNESS

So far, we have considered constant liquid–gas and solid–liquid interfacial tensions γ_G and γ_L, respectively, which are not measurable in reality. An adsorption layer at the interfaces, caused by intermolecular forces,[23] in which the molecular organization differs from that in the bulk,[24,25] affects the interfacial tensions. This is why, in previous literature[11,26,27] and in the following, the interfacial tensions are treated as functions of the volume fractions at the adsorption layer.

Multiple equilibrium contact angles are frequently observed in experiments and arise, for example due to heterogeneity, deformation, and adaption.[28] In addition, macroscopic roughness,[27,29] which is associated with structural deformation of the solid substrate, contributes to this behavior. The contact angle hysteresis $\mathrm{CAH} := \theta_{adv} - \theta_{rec}$ is defined as the difference between the advancing contact angle θ_{adv} and the receding contact angle θ_{rec}, which represent the maximum and minimum contact angles at the

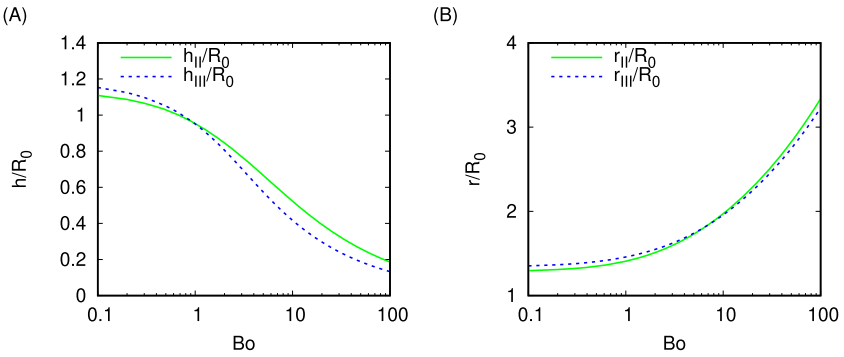

FIG. 14. (a) Ratio of the droplet height to the initial droplet radius of the oblate spheroidal cap h_{II}/R_0 (green) and the pancake shape h_{III}/R_0 (blue). (b) Ratio of the base radius to the initial droplet radius of the oblate spheroidal cap r_{II}/R_0 (green) and the pancake shape r_{III}/R_0 (blue).

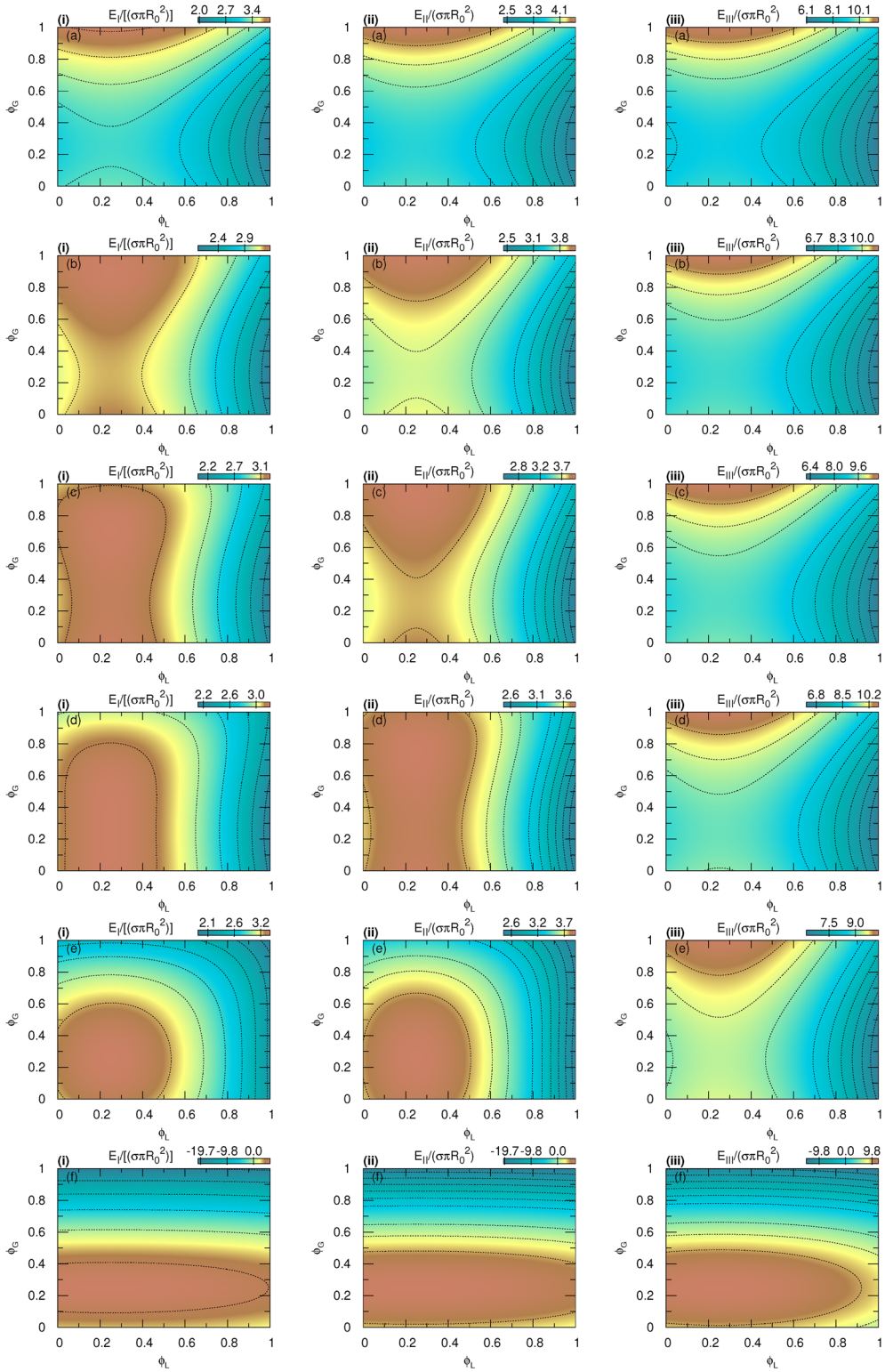

FIG. 16. Energy landscape $E(\phi_L, \phi_G)$ with $\sigma = 0.0728 \frac{\mathrm{N}}{\mathrm{m}}$, $\Delta\rho = 998 \frac{\mathrm{kg}}{\mathrm{m}^3}$, $g = 9.81 \frac{\mathrm{m}}{\mathrm{s}^2}$, (i) Bo = 0.1, (ii) Bo = 1, and (iii) Bo = 20 and (a) $S/R_0^2 = 0$, (b) $S/R_0^2 = 3$, (c) $S/R_0^2 = 4$, (d) $S/R_0^2 = 5$, (e) $S/R_0^2 = 8$, and (f) $S/R_0^2 = 150$.

equilibrium state, respectively. On a macroscopically smooth solid substrate, Young's law is not able to explain the contact angle hysteresis occurring in experiments, when considering constant interfacial tensions. To comprehend this, we incorporate microscopic roughness by varying the liquid–solid and solid–gas interfacial tensions as functions of surface compositions, following Ref. 26. The local energy minima of the total free energy, dependent on the volume fractions at the solid–liquid and solid–gas interfaces, respectively, correspond to the equilibrium compositions at the adsorption layer. Several energy minima with distinct Young's contact angles result in the occurrence of contact angle hysteresis.[11,26,27]

In the following, we analyze energy landscapes $E(\phi_L, \phi_G)$ with varying liquid–solid and solid–gas interfacial tensions. Here,

$$\phi_L = \frac{V_{LL}}{V_{LL} + V_{GL}}$$

and

$$\phi_G = \frac{V_{LG}}{V_{LG} + V_{GG}}$$

represent the volume fraction of the liquid species in the adsorption layer at the solid–liquid and the solid–gas interfaces, respectively. The parameters V_{LL}, V_{GL}, V_{LG}, and V_{GG} are defined as follows:

- V_{LL}: volume of the liquid in the adsorption layer beneath the liquid droplet;
- V_{GL}: volume of the gas in the adsorption layer beneath the liquid droplet;
- V_{LG}: volume of the liquid in the adsorption layer under the gas phase;
- V_{GG}: volume of gas in the adsorption layer under the gas phase.

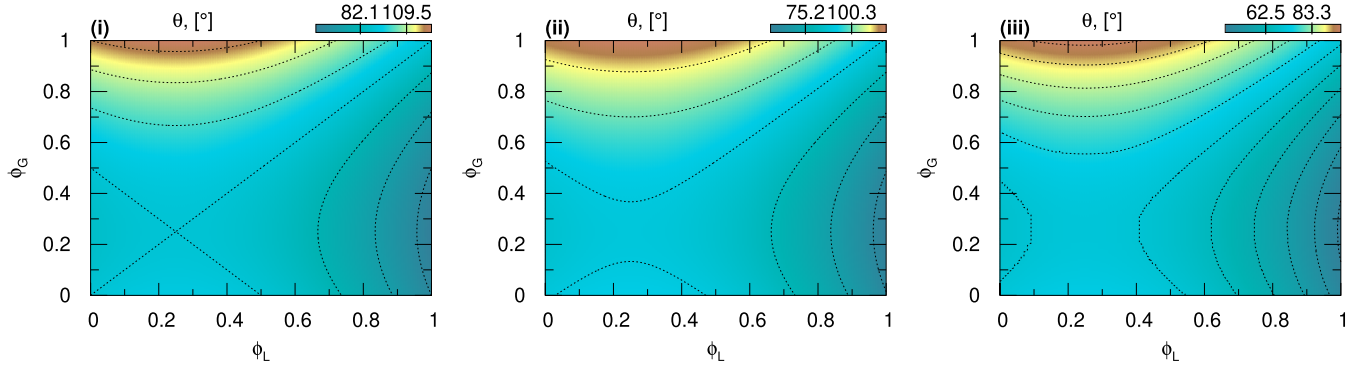

FIG. 17. Macroscopic contact angles $\theta(\phi_L, \phi_G)$ corresponding to the minimal energy for (i) Bo = 0.1 (spherical cap), (ii) Bo = 1 (oblate spheroidal cap), and (iii) Bo = 20 (pancake shape) with $\sigma = 0.0728 \frac{\mathrm{N}}{\mathrm{m}}$, $\Delta\rho = 998 \frac{\mathrm{kg}}{\mathrm{m}^3}$, $g = 9.81 \frac{\mathrm{m}}{\mathrm{s}^2}$.

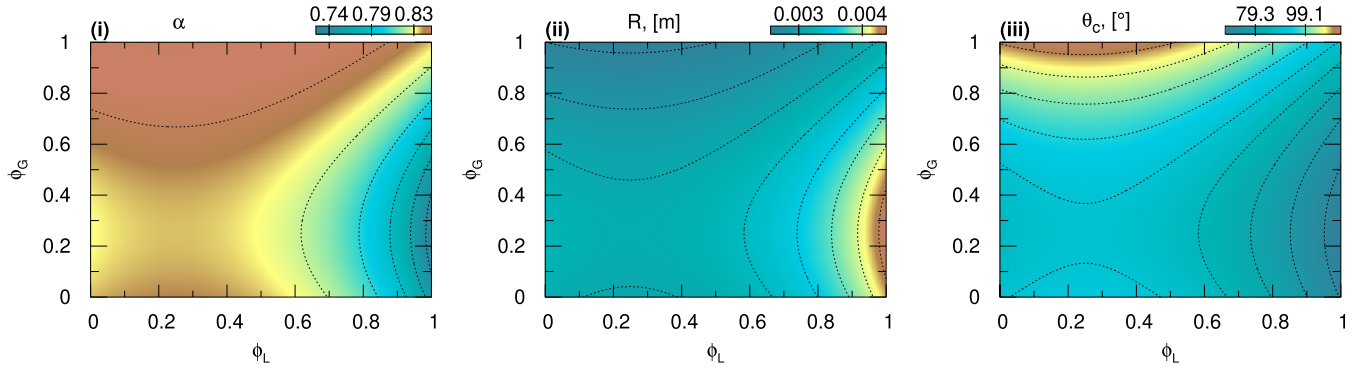

FIG. 18. (i) $\alpha(\phi_L, \phi_G)$, (ii) $R(\phi_L, \phi_G)$, and (iii) $\theta_c(\phi_L, \phi_G)$ corresponding to the minimal energy of the oblate spheroidal cap (Bo = 1) with $\sigma = 0.0728 \frac{\mathrm{N}}{\mathrm{m}}$, $\Delta\rho = 998 \frac{\mathrm{kg}}{\mathrm{m}^3}$, $g = 9.81 \frac{\mathrm{m}}{\mathrm{s}^2}$.

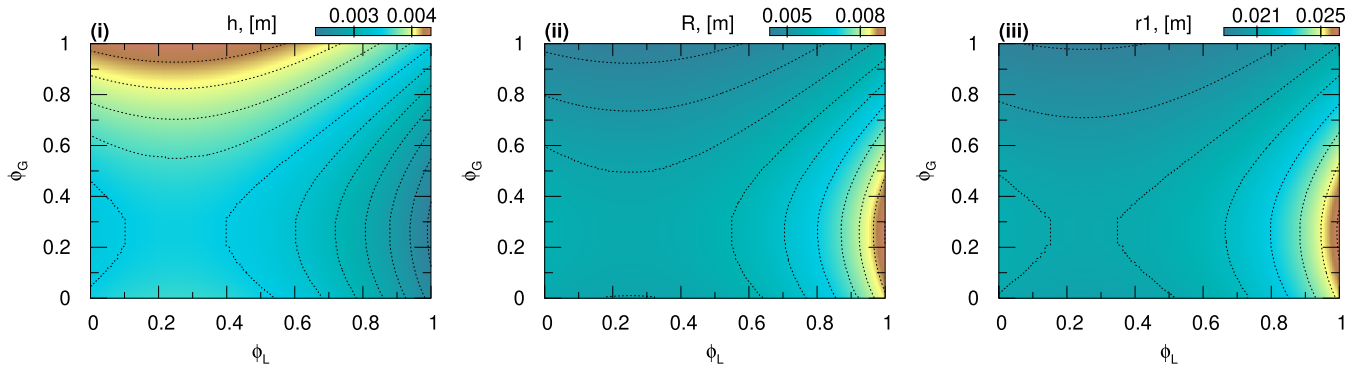

FIG. 19. (i) $h(\phi_L, \phi_G)$, (ii) $R(\phi_L, \phi_G)$, and (iii) $r_1(\phi_L, \phi_G)$ corresponding to the minimal energy of the pancake shape (Bo = 20) with $\sigma = 0.0728 \frac{\mathrm{N}}{\mathrm{m}}$, $\Delta\rho = 998 \frac{\mathrm{kg}}{\mathrm{m}^3}$, $g = 9.81 \frac{\mathrm{m}}{\mathrm{s}^2}$.

In Sec. IV, we use non-constant interfacial tensions $\gamma(\phi_L)$ in place of γ_L and $\gamma(\phi_G)$ instead of γ_G. We define $\gamma(\phi) = \gamma_2\phi^2 + \gamma_1\phi + \gamma_0$ as a quadratic function. The coefficients $\gamma_2 = -\ell\chi$, $\gamma_1 = \ell\chi\left(1 - \frac{\Delta p - \Delta\chi}{\chi}\right)$, and $\gamma_0 = \ell\chi\frac{p_G + \chi_G}{\chi}$ are related to the internal energy Δp, internal energies of the gas phase p_G, adsorption layer depth ℓ, and the difference in the van der Waals force $\Delta\chi$ of the liquid–solid and gas–solid χ_G. Here, the interfacial tensions are calculated as

$$\gamma(\phi) = 2\sigma\left(-\phi^2 + \frac{1}{2}\phi\right),$$

and the total energy is given by

$$E(\phi_L, \phi_G) = \sigma S_{LG} - (\gamma(\phi_G) - \gamma(\phi_L))S_{SL} + \gamma_G S + \Delta\rho g\bar{z}V, \qquad (12)$$

where θ corresponds to the macroscopic contact angle used implicitly in the formulation of Eq. (12). The energy landscapes shown in Fig. 16(i) for the spherical cap agree with Ref. 11. The energy landscapes in Fig. 16(ii) for the oblate spheroidal cap have a similar qualitative trend, with equivalent positions of the local minima but with a slower progression in S/R_0^2 than those of the spherical cap in Fig. 16(i). In addition, in Fig. 16(iii), the energy landscapes of the pancake shape show an even slower progression. A dependency of the contact angle hysteresis on the droplet size arises due to the scaling of the function that depends on the ratio of the surface area of the solid substrate and the droplet size S/R_0^2, as shown in Ref. 11, in both the horizontal and vertical directions.

Figure 17 shows the macroscopic contact angles $\theta(\phi_L, \phi_G)$ of the spherical cap, the oblate spheroidal cap, and the pancake shape. No significant qualitative differences are observed between the three figures, aside from quantitative differences. Figure 18 shows the geometrical parameters $\alpha(\phi_L, \phi_G)$, $R(\phi_L, \phi_G)$, and $\theta_c(\phi_L, \phi_G)$ of the oblate spheroidal cap corresponding to the minimum energy. The geometrical parameters $h(\phi_L, \phi_G)$, $R(\phi_L, \phi_G)$, and $r_1(\phi_L, \phi_G)$ associated with the energy-minimizing pancake shape are depicted in Fig. 19.

V. COMPARISON BETWEEN THE THEORETICAL DROPLET EQUILIBRIA AND THE NUMERICAL RESULTS OBTAINED USING THE ALLEN-CAHN MODEL

Figures 20 and 21 show the numerical results obtained using the Allen–Cahn model[15] for different Bond numbers and various values of $\Delta\gamma/\sigma$. The black curves represent the estimated liquid–gas interface derived from the previously examined theoretical calculations by applying the equilibrium parameters α and R of the oblate spheroidal cap and the equilibrium parameters r_1 and R of the pancake shape. A good match is observed between the liquid–gas interface in the numerical work and the theoretically predicted liquid–gas interface.

To calculate the contact angle in the numerical work, we first determine the intersection curve of the liquid and the gas phases at $\phi = 0.5$ using bilinear interpolation.

Figure 22 shows both measurement methods used to calculate the contact angle in the numerical work, given in Table I. The measured microscopic contact angle, represented in Fig. 22(a), is obtained by selecting the intersection point of the liquid–gas interface and the solid substrate (x_1, z_1) and a second point on the liquid–gas interface near the first point (x_2, z_2). The measured microscopic contact angle is calculated using the gradient angle: $\theta_{\mathrm{sim,a}} = \arctan\left(\frac{z_2 - z_1}{x_2 - x_1}\right)$. The second method, used to determine the measured macroscopic contact angle and shown in Fig. 22(b), involves solving the volume constraint $V = V(r, h, \theta_{\mathrm{sim,b}})$ of the respective droplet shape. This equation, which depends on the base radius r and the height of the droplet h, is solved to determine the contact angle $\theta_{\mathrm{sim,b}}$. Measured microscopic contact angles may depend on the resolution, as it requires zooming in close to the three-phase contact line. In contrast, measured macroscopic contact

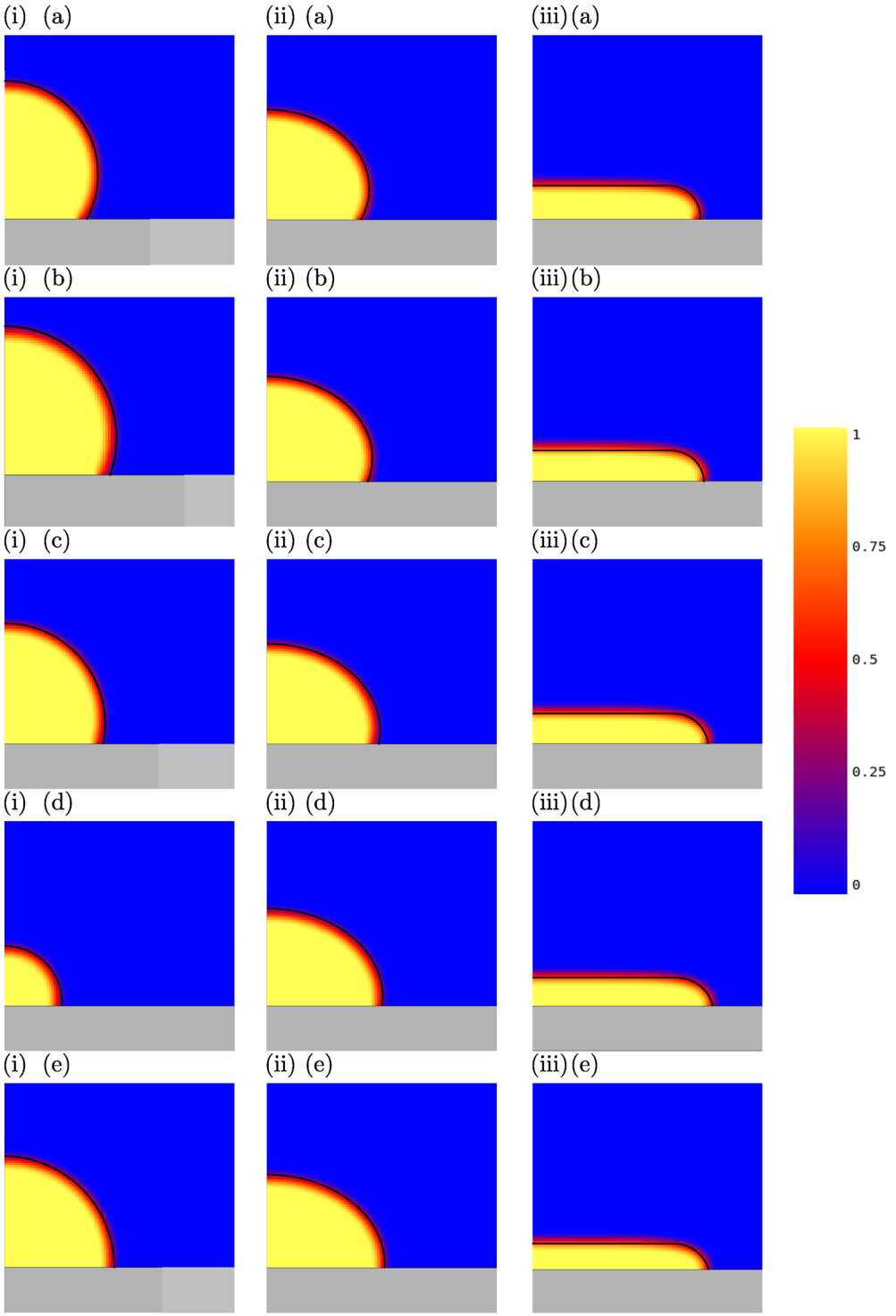

FIG. 20. Numerical results and theoretically estimated interface (black line) for $\sigma = 0.0728 \frac{\mathrm{N}}{\mathrm{m}}$, $\Delta\rho = 998 \frac{\mathrm{kg}}{\mathrm{m}^3}$, $g = 9.81 \frac{\mathrm{m}}{\mathrm{s}^2}$, (i) Bo = 0.1, (ii) Bo = 1, (iii) Bo = 20, and for (a) $\Delta\gamma/\sigma = -0.5625$, (b) $\Delta\gamma/\sigma = -0.42$, (c) $\Delta\gamma/\sigma = -0.28$, (d) $\Delta\gamma/\sigma = -0.14$, and (e) $\Delta\gamma/\sigma = -0.0625$.

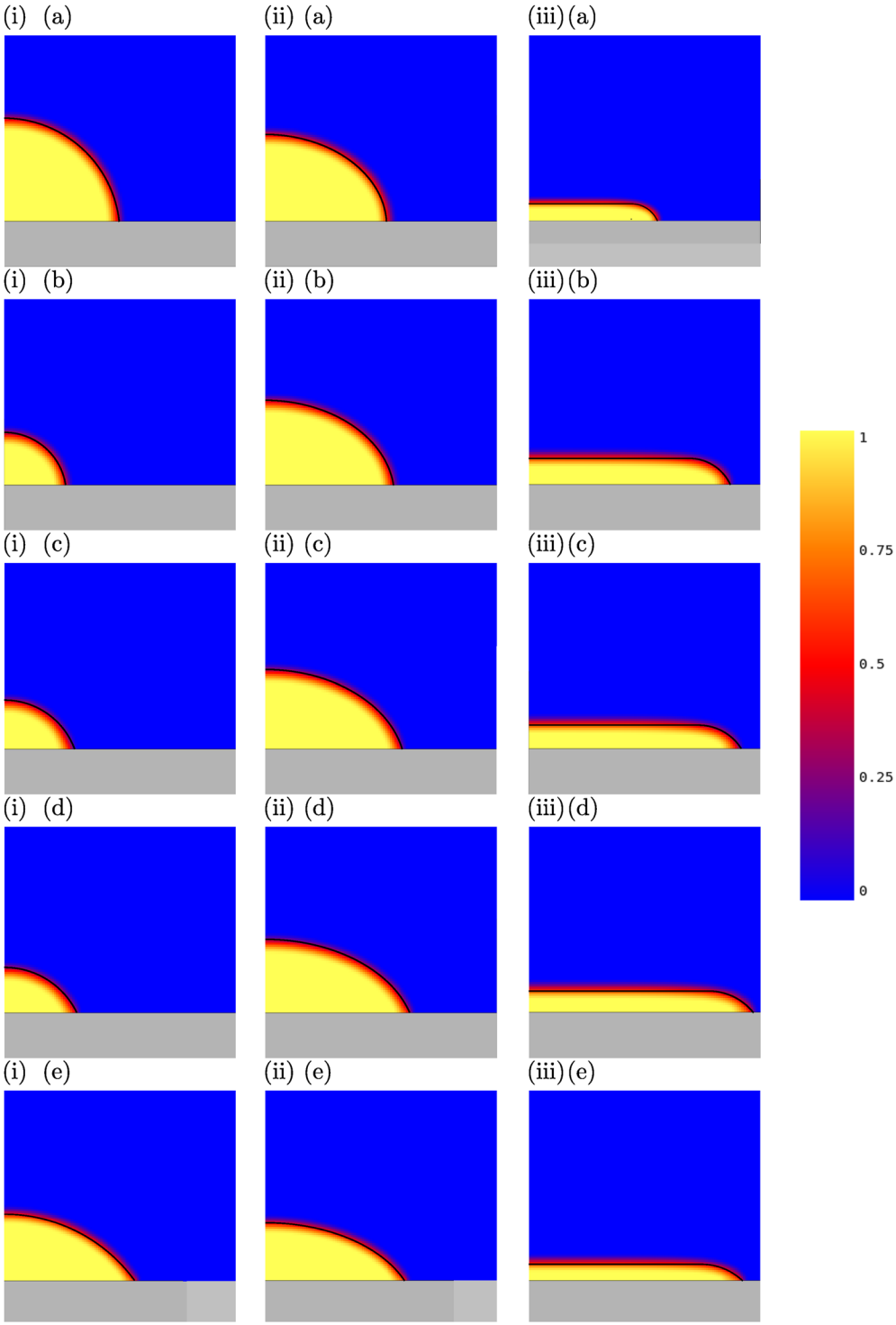

FIG. 21. Numerical results and theoretically estimated interface (black line) for $\sigma = 0.0728 \frac{\mathrm{N}}{\mathrm{m}}$, $\Delta\rho = 998 \frac{\mathrm{kg}}{\mathrm{m}^3}$, $g = 9.81 \frac{\mathrm{m}}{\mathrm{s}^2}$, (i) Bo = 0.1, (ii) Bo = 1, (iii) Bo = 20, and for (a) $\Delta\gamma/\sigma = 0.0625$, (b) $\Delta\gamma/\sigma = 0.14$, (c) $\Delta\gamma/\sigma = 0.28$, (d) $\Delta\gamma/\sigma = 0.42$, and (e) $\Delta\gamma/\sigma = 0.5625$.

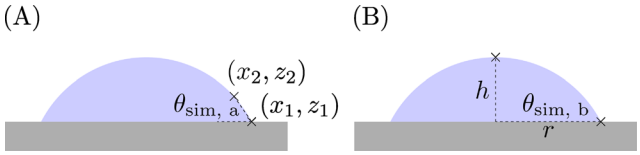

FIG. 22. Schematics of the measurement of the (a) measured microscopic contact angle determined by $\theta_{\text{sim, a}} = \arctan\left(\frac{z_2 - z_1}{x_2 - x_1}\right)$ and (b) measured macroscopic contact angle obtained by measuring the droplet height h and the base radius r and by solving the volume constraint $V = V(r, h, \theta_{\text{sim, b}})$ of the respective droplet shape.

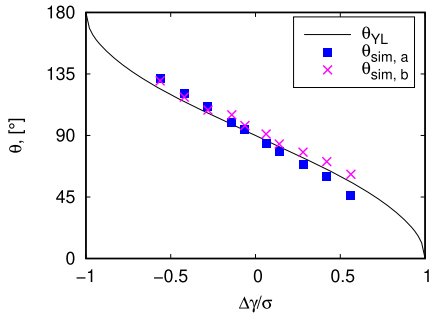

FIG. 23. Contact angles according to Young's law θ_{YL} (black line) compared to the measured microscopic contact angles $\theta_{\text{sim, a}}$ (blue squares) and the measured macroscopic contact angles $\theta_{\text{sim, b}}$ (pink crosses) obtained from the numerical work of the spherical cap with Bo = 0.1 for different values of $\Delta\gamma/\sigma$.

angles are independent of the resolution and yield consistent results for identical setups.

In Fig. 23, there is a good agreement of the measured microscopic and macroscopic contact angles obtained from the Allen–Cahn model of a spherical cap (Bo = 0.1) and the predictions of Young's law. The measured macroscopic contact angles exhibit a closer match to Young's law than the measured microscopic contact angles, as also observed in Ref.15.

In Fig. 24(i), for Bo = 1, the apparent contact angles θ, the imaginary contact angles θ_c, and the parameter α from the Allen–Cahn model show a closer agreement with the curves obtained via energy minimization (green line) than those in Fig. 24(ii) for Bo = 3. This suggests that the oblate spheroidal cap model more accurately represents the droplet shape for Bo = 1 than for Bo = 3.

Figure 24(a)(ii) demonstrates a good agreement between the measured microscopic contact angles (blue squares) of the oblate spheroidal cap (Bo = 3) and the macroscopic contact angles (green line), as well as the predictions of Young's law (black line). However, the measured macroscopic contact angles (pink crosses) show a greater deviation from the green line. In Fig. 24(b)(ii), a noticeable discrepancy is observed between the imaginary contact angles θ_c predicted by energy minimization (green line) and the imaginary contact angles obtained from the Allen-Cahn model. Furthermore, in Fig. 24(c)(ii), a deviation is observed between the parameter α computed via energy minimization (green line) and the measured macroscopic contact angles from the Allen–Cahn model (pink crosses).

For the pancake shape (Bo = 20) in Fig. 25, the measured macroscopic contact angles (pink crosses) exhibit a closer agreement with the macroscopic contact angles (green line) compared to the measured microscopic contact angles (blue squares), which align more closely with Young's law. This illustrates a key advantage of macroscopic over microscopic contact angles, as their measured values remain unaffected by the resolution.

TABLE I. Measured microscopic contact angles $\theta_{\text{sim, a}}$ and measured macroscopic contact angles $\theta_{\text{sim, b}}$ obtained from numerical work for Bo = 0.1 (spherical cap), Bo = 1 (oblate spheroidal cap), Bo = 3 (oblate spheroidal cap), and Bo = 10 (pancake shape) with $\sigma = 0.0728 \frac{\text{N}}{\text{m}}$.

	Bo = 0.1		Bo = 1		Bo = 3		Bo = 20	
$\Delta\gamma$	$\theta_{\text{sim, a}}$	$\theta_{\text{sim, b}}$	$\theta_{\text{sim, a}}$	$\theta_{\text{sim, b}}$	$\theta_{\text{sim, a}}$	$\theta_{\text{sim, b}}$	$\theta_{\text{sim, a}}$	$\theta_{\text{sim, b}}$
−0.040 95	131.57°	123.46°	129.85°	119.67°	130.21°	123.51°	126.51°	105.36°
−0.030 576	120.85°	114.51°	119.92°	112.24°	118.45°	117.43°	116.42°	92.47°
−0.020 384	111.14°	105.46°	109.81°	105.29°	109.19°	112.31°	106.38°	90.22°
−0.010 192	99.40°	99.95°	99.43°	97.68°	98.81°	107.03°	95.94°	83.00°
−0.004 55	94.05°	93.76°	93.66°	95.49°	92.93°	104.03°	90.20°	82.59°
0.004 55	83.78°	89.52°	83.54°	89.61°	83.54°	99.77°	80.38°	73.40°
0.010 192	78.42°	83.29°	77.95°	84.94°	77.98°	99.93°	74.69°	66.14°
0.020 384	68.98°	77.27°	68.49°	77.53°	67.20°	91.48°	63.81°	62.05°
0.030 576	59.76°	67.95°	59.56°	69.20°	57.08°	89.20°	58.45°	56.38°
0.040 95	45.80°	57.34°	51.10°	60.06°	46.64°	82.94°	48.08°	49.64°

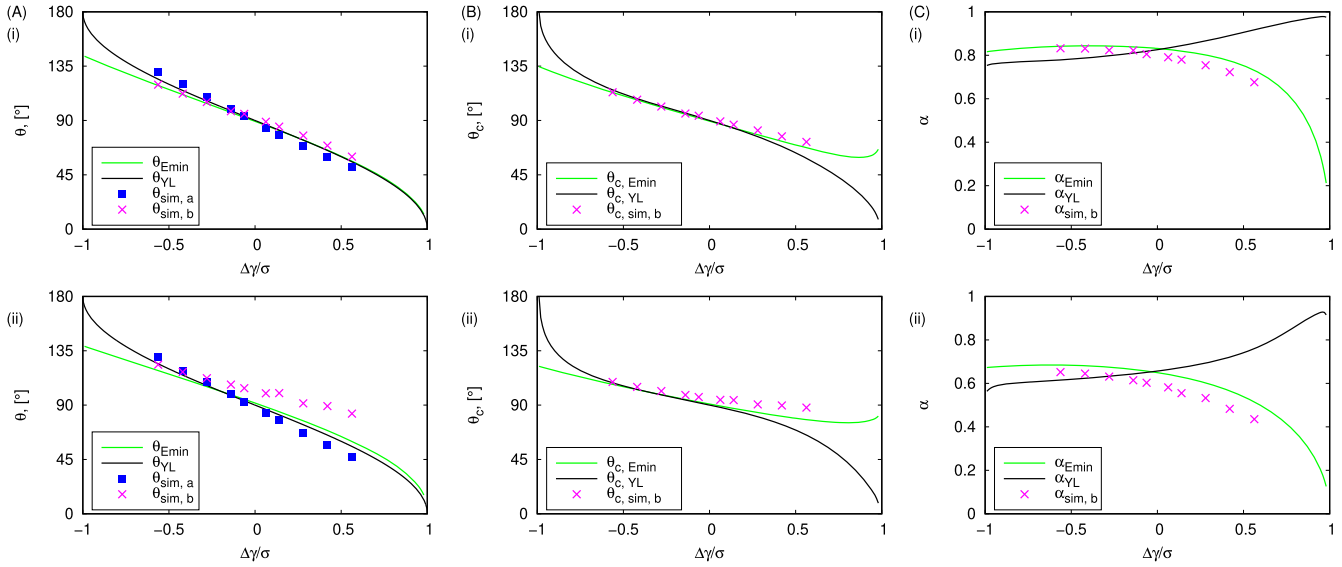

FIG. 24. (a) Macroscopic contact angles of the oblate spheroidal cap obtained from energy minimization θ_{Emin} (green line) for (i) Bo = 1 and (ii) Bo = 3 and Young's law θ_{YL} (black line) as a function of $\Delta\gamma/\sigma$ compared to the measured microscopic contact angles $\theta_{sim,\,a}$ (blue squares) and the measured macroscopic contact angles $\theta_{sim,\,b}$ obtained from the Allen–Cahn model (pink crosses) for different values of $\Delta\gamma/\sigma$. (b) Imaginary contact angles $\theta_{c,\,Emin}$ of the oblate spheroidal cap as a function of $\Delta\gamma/\sigma$ (green line) compared to the imaginary measured macroscopic contact angles $\theta_{c,\,sim,\,b}$ (pink crosses) obtained from the Allen–Cahn model for different values of $\Delta\gamma/\sigma$ for (i) Bo = 1 and (ii) Bo = 3. (c) Parameter α_{Emin} from energy minimization (green line) and α_{YL} from Young's law (black line) as a function of $\Delta\gamma/\sigma$ compared to $\alpha_{sim,\,b}$ from the Allen–Cahn model and the measured macroscopic contact angles (pink crosses) for (i) Bo = 1 and Bo = 3.

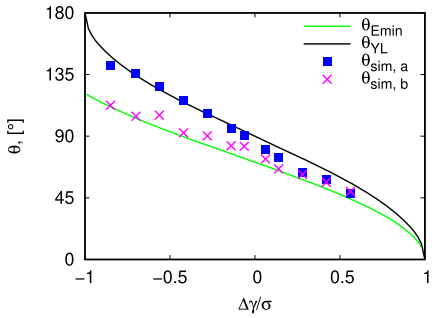

FIG. 25. Macroscopic contact angles of the pancake shape obtained from energy minimization θ_{Emin} (green) for Bo = 20 and from Young's law θ_{YL} (black) as a function of $\Delta\gamma/\sigma$, compared to the measured microscopic contact angles $\theta_{sim,\,a}$ (blue squares) and the measured macroscopic contact angles $\theta_{sim,\,b}$ (pink crosses) obtained from the Allen–Cahn model for Bo = 20 at different values of $\Delta\gamma/\sigma$.

VI. CONCLUSION

In conclusion, we have examined three distinct shapes of the liquid droplet in relation to the gravitational influence on the wetting phenomenon on smooth solid substrates: the spherical cap, the oblate spheroidal cap, and the pancake shape. We utilized formulas for the liquid–gas and the liquid–solid interfacial areas, the volume, and the height of the centroid for each droplet shape to calculate the total energy and determine the macroscopic contact angles through energy minimization by approximating the droplet shape by a geometric model. For small values of the Bond number, the droplet is approximately a spherical cap, the body energy can be neglected, and the macroscopic contact angle can be simply expressed using Young's law $\cos\theta_{YL} = \Delta\gamma/\sigma$ and the liquid–solid, solid–gas, and liquid–gas interfacial tensions.

However, as the droplet size increases with $Bo < Bo^*$, the droplet adopts the shape of an oblate spheroidal cap and the macroscopic contact angle remains close to that predicted by Young's law. As the Bond number exceeds Bo^*, the droplet assumes the shape of a pancake. Since the transition of the droplet shape from the oblate spheroidal cap to the pancake shape at Bo^* is discontinuous, we assume that a continuous transition between these shapes occurs in a neighborhood around Bo^*. At this state, significant deviations of the macroscopic contact angles from Young's law can be observed. The macroscopic contact angles of the oblate spheroidal cap and the pancake shape cannot simply be derived by a closed equation dependent on the solid–liquid, solid–gas, and liquid–gas interfacial tensions, as Young's law. These contact angles are also dependent on the droplet volume, the density difference of the liquid and gas phases, and the gravitational acceleration and are calculated numerically. As the gravitational effect increases, which corresponds to increasing the droplet size, the droplet becomes more deformed, becoming flatter and wider.

The Bond number Bo^*, at which the transition between the oblate spheroidal cap and the pancake shape occurs, decreases as $\Delta\gamma/\sigma$ increases and is, therefore, dependent on the surface tensions, which also determine the approximated droplet shape. The contact angle hysteresis on a smooth solid, caused by varying the interfacial tensions in order to include intermolecular rearrangements of

liquid and gas species at the adsorption layer at the microscopic scale, is also dependent on the droplet size, as demonstrated by the local energy minima in the energy landscapes. By comparing the shapes and contact angles from the Allen–Cahn model[15] with the theoretical predictions, we have validated our theory. For large droplets, the measured microscopic contact angles, which depend on the resolution at the triple junction, exhibit better agreement with the theoretical microscopic contact angles, whereas the measured macroscopic contact angles, independent of the resolution, correspond more closely to the theoretical macroscopic contact angles. This behavior is in contrast to small droplets, for which the measured macroscopic contact angles more closely approximate microscopic contact angles than measured microscopic contact angles.[15] This suggests that the appropriate method for contact angle determination depends on the droplet size.

VII. OUTLOOK

Since we have only considered a smooth solid substrate, including microscopic roughness, macroscopic roughness, and the Cassie–Baxter and the Wenzel states could also be incorporated.[27] The ratio $\upsilon \in [\upsilon_{\min}, \upsilon_{\max}]$ of the liquid–solid contact area in the considered state to that on a smooth solid substrate with an analogous setting defines the transition from the Cassie–Baxter to the Wenzel state and describes, how much gas remains trapped under the droplet. By modifying the interfacial areas, neglecting the volume of the liquid penetrating into the roughness structure of the solid surface, as well as its effect on the height of the centroid $\bar{z}$, and neglecting any curvature of the liquid–gas interfaces below the droplet, we obtain a free energy that depends on three parameters $E(\theta, \alpha, \upsilon)$ for the oblate spheroidal cap model and $E(\theta, h, \upsilon)$ for the pancake model, leading to a three-dimensional energy minimization. The parameter $\upsilon = \upsilon_{\min}$ corresponds to the Cassie–Baxter state, where the droplet does not penetrate into the macroscopic roughness structure of the solid surface. Here, the modified liquid–gas and solid–liquid interfacial areas are given by

$$\tilde{S}_{LG} = S_{LG} + (1 - \Phi) S_{SL}$$

and

$$\tilde{S}_{SL} = \Phi S_{SL},$$

where Φ represents the surface fraction covered by the droplet in the Cassie–Baxter state.

The Wenzel state with $\upsilon = \upsilon_{\max}$ represents full coverage of the solid surface by the liquid under the droplet. Here, the roughness of the solid surface is characterized by the ratio of the real surface to its projection onto the horizontal plane, denoted by $f > 1$. The solid–gas interface area is modified by $\tilde{S}_{SG} = f S_{SG}$, while the liquid–gas interfacial area $\tilde{S}_{LG} = S_{LG}$ remains unchanged. In both states, the formulas for the interfacial areas, the volume, and the height of the centroid of the oblate spheroidal cap and the pancake shape can be substituted, and the energy

$$E = \sigma \tilde{S}_{LG} - \Delta\gamma \tilde{S}_{SL} + \Delta\rho g V \bar{z}$$

can be minimized. By restricting the analysis to these two states, the problem is reduced to a two-dimensional minimization, $E(\theta, \alpha;\ \upsilon)$ or $E(\theta, h;\ \upsilon)$, respectively. Contact angle hysteresis is expected, caused by macroscopic roughness and distinct contact angles in the Cassie–Baxter and Wenzel states. The described concept is based on

the work in Ref. 29 for spherical cap droplets and could be extended to oblate spheroidal caps and pancake shapes.

A greater impact of gravity on a gas bubble in the liquid phase on a solid substrate is expected compared to the liquid droplet investigated in this study. The equilibrium shape of the gas bubbles and their corresponding contact angles could be compared to those of the liquid droplet. By neglecting gravitational energy and focusing on small droplets, no significant difference between the liquid droplet and the gas bubble is observed.[11]

The significant deviations between the microscopic contact angles and the macroscopic contact angles derived from the pancake shape model for large droplets, as observed in this study, may decrease for a different geometric model. One possibility is to model the edge of the pancake shape with an elliptical torus, whose cross-section in the x–z plane is elliptical rather than circular. Such a representation requires a three-dimensional free energy minimization and increases the mathematical complexity significantly.

ACKNOWLEDGMENTS

F.A. acknowledged Gottfried-Wilhelm Leibniz Prize Grant No. NE 822/31-1 of the German Research Foundation (DFG) for funding this research. F.W. was grateful to VirtMat Project P09 of the Helmholtz Association (MSE-Programme No. 43.31.01).

AUTHOR DECLARATIONS

Conflict of Interest

The authors have no conflicts to disclose.

Author Contributions

Franziska Aurbach: Formal analysis (lead); Investigation (lead); Methodology (equal); Validation (lead); Visualization (lead); Writing – original draft (lead). **Fei Wang**: Conceptualization (lead); Methodology (equal); Supervision (lead); Writing – review & editing (equal). **Britta Nestler**: Funding acquisition (lead); Project administration (lead); Writing – review & editing (equal).

DATA AVAILABILITY

Data sharing is not applicable to this article as no new data were created or analyzed in this study.

APPENDIX A: SURFACE OF THE LIQUID–GAS INTERFACE OF THE OBLATE OBLATE SPHEROIDAL CAP

The following derivation applies to an oblate spheroidal cap with $0 < \alpha < 1$. We describe the oblate spheroidal contour using the following parametric equation:

$$\alpha^3 x^2 + (z - \alpha R)^2 = \alpha^2 R^2,$$
$$x = \frac{\sqrt{\alpha z(2\alpha R - z)}}{\alpha^2},$$
$$\frac{\mathrm{d}x}{\mathrm{d}z} = \frac{\alpha(2\alpha R - z) - \alpha z}{2\alpha^2\sqrt{\alpha z(2\alpha R - z)}}.$$

First, we use the solid of revolution around the z-axis to obtain the surface area of the entire oblate spheroid,

$$\begin{aligned} S &= 2\int_0^{R\alpha} 2\pi x\sqrt{1+\left(\frac{dx}{dz}\right)^2}\,\mathrm{d}z \\ &= 4\pi\int_0^{R\alpha} \frac{\sqrt{\left(1-\alpha^3\right)z^2 + \left(2R\alpha^4 - 2\alpha R\right)z + \alpha^2R^2}}{\alpha^3}\mathrm{d}z \\ &= \frac{2\left(\operatorname{arcsinh}\left(\frac{\sqrt{1-\alpha^3}}{\alpha^{\frac{3}{2}}}\right)\alpha^3 + \sqrt{1-\alpha^3}\right)R^2\pi}{\sqrt{1-\alpha^3}\alpha}. \end{aligned}$$

The surface area of the oblate spheroid truncated by the solid substrate can be expressed as

$$\begin{aligned} \tilde{S} &= \int_0^{R\alpha(1+\cos\theta_c)} 2\pi x\sqrt{1+\left(\frac{dx}{dz}\right)^2}\,\mathrm{d}z \\ &= 2\pi\int_0^{R\alpha(1+\cos\theta_c)} \frac{\sqrt{\left(1-\alpha^3\right)z^2 + \left(2R\alpha^4 - 2\alpha R\right)z + \alpha^2R^2}}{\alpha^3}\mathrm{d}z \\ &= -\omega\left(\alpha^3\left(\operatorname{arcsinh}\left(\frac{\psi\phi}{\alpha^{\frac{3}{2}}}\right) + \operatorname{arcsinh}\left(\frac{\psi}{\alpha^{\frac{3}{2}}}\right)\right) + \nu + \psi\right). \end{aligned}$$

By subtracting the truncated surface $\tilde{S}$ from S, we obtain the surface area of the oblate spheroidal cap $S_c = S - \tilde{S}$ as

$$S_c = \omega\left(\alpha^3\left(\operatorname{arcsinh}\left(\frac{\psi\phi}{\alpha^{\frac{3}{2}}}\right) - \operatorname{arcsinh}\left(\frac{\psi}{\alpha^{\frac{3}{2}}}\right)\right) + \nu - \psi\right),$$

with $\nu = \psi\sqrt{-\left(\cos^2(\theta_c)\right)\alpha^3 + \alpha^3 + \cos^2(\theta_c)}\phi$, $\psi = \sqrt{1-\alpha^3}$, $\phi = \cos(\theta_c)$, and $\omega = -\frac{R^2\pi}{\psi\alpha}$.

APPENDIX B: VOLUME OF THE OBLATE SPHEROIDAL CAP

In order to calculate the total energy for the droplet formed as an oblate spheroidal cap, we need an expression for the volume of the oblate spheroidal cap. In the first step, we distinguish between two cases for the imaginary contact angle: $\pi/2 < \theta_c < \pi$ and $0 < \theta_c < \pi/2$. First, we consider the case of imaginary contact angles where $\pi/2 < \theta_c < \pi$,

$$\begin{aligned} \zeta + \frac{\pi}{2} &= \theta_c, \\ \beta + \zeta + \frac{\pi}{2} &= \pi, \\ \beta &= \frac{\pi}{2} - \zeta \\ &= \pi - \theta_c, \\ z_1 = R\sin\zeta &= R\sin\left(\theta_c - \frac{\pi}{2}\right) \\ &= -R\cos\theta_c, \\ b = R - z_1 &= R + R\cos\theta_c = R(1+\cos\theta_c). \end{aligned}$$

In the following, we include imaginary contact angles where $0 < \theta_c < \pi/2$:

$$z_1 = R - (2R - b) = -R + b,$$
$$b = z_1 + R,$$
$$\theta_c + \beta + \frac{\pi}{2} = \pi,$$
$$\zeta + \beta + \frac{\pi}{2} = \pi,$$
$$\theta_c = \zeta,$$
$$z_1 = R\cos\zeta = R\cos\theta_c,$$
$$b = R(1 + \cos\theta_c).$$

The volume of the spherical cap with the contour line,

$$(z - (R - b + \alpha b))^2 + x^2 = R^2,$$

truncated to form the contact angle θ_c, can be calculated as

$$\begin{aligned}
V &= \pi\int_{\alpha b}^{2R-b+\alpha b} x^2 \mathrm{d}z \\
&= \pi\int_{\alpha b}^{2R-b+\alpha b} R^2 - (z - (R - b + \alpha b))^2 \mathrm{d}z \\
&= \pi\int_{0}^{2R-b} R^2 - (z - (R - b))^2 \mathrm{d}z \\
&= \pi\int_{0}^{2R-b} -z^2 + 2(R - b)z + 2Rb - b^2 \mathrm{d}z \\
&= \pi\left(-\frac{1}{3}(2R - b)^3 + (R - b)(2R - b)^2 + b(2R - b)^2\right) \\
&= \pi\left(\frac{4}{3}R^3 - Rb^2 + \frac{1}{3}b^3\right) \\
&= \frac{\pi R^3}{3}(1 - \cos\theta_c)^2(2 + \cos\theta_c).
\end{aligned}$$

The volume of the spherical cap is equivalent to that of the oblate spheroidal cap.

APPENDIX C: HEIGHT OF THE CENTROID OF THE OBLATE SPHEROIDAL CAP

To calculate the body energy of the oblate spheroidal cap, we need the height of its centroid, which is given by $\bar{z} = \int_V \frac{z}{V}\mathrm{d}z$,

$$\begin{aligned}
\bar{z} &= \frac{1}{V}\int_{\alpha(1+\omega)R}^{2\alpha R} \pi x^2 z \mathrm{d}z - \alpha(1 + \omega)R \\
&= \frac{1}{V}\int_{\alpha(1+\omega)R}^{2\alpha R} \pi\frac{z^2(2\alpha R - z)}{\alpha^3}\mathrm{d}z - \alpha(1 + \omega)R \\
&= \frac{\pi(\alpha R)^4}{\alpha^3 V}\left[\frac{4}{3} - \frac{2}{3}(1 + \omega)^3 + \frac{1}{4}(1 + \omega)^4\right] - \alpha(1 + \omega)R \\
&= \frac{3\pi\alpha R^4}{12\pi R^3}\frac{(3\omega^2 + 10\omega + 11)(1 - \omega)^2}{(1 - \omega)^2(2 + \omega)} - \alpha(1 + \omega)R \\
&= \frac{\alpha R(3\omega^2 + 10\omega + 11)}{4(2 + \omega)} - \alpha(1 + \omega)R \\
&= \frac{\alpha R(1 - \cos\theta_c)(3 + \cos\theta_c)}{4(2 + \cos\theta_c)},
\end{aligned}$$

with $\omega = \cos\theta_c$.

APPENDIX D: APPARENT AND IMAGINARY CONTACT ANGLES OF THE OBLATE SPHEROIDAL CAP

The contact angle of the oblate spheroidal cap θ can be expressed in terms of the imaginary contact angle of the corresponding spherical cap θ_c and the parameter α. The oblate spheroidal cap and the spherical cap are visualized in Fig. 26 by the blue line and the red dashed line, respectively. To begin, we consider the parametric equation of the ellipse,

$$\alpha^3 x^2 + (z - \alpha R)^2 = \alpha^2 R^2.$$

By differentiating, we obtain the following:

$$\begin{aligned}
2\alpha^3 x + 2zz' - 2\alpha R z' &= 0, \\
\alpha^3 x &= z'(\alpha R - z), \\
z' &= \frac{\alpha^3 x}{\alpha R - z}.
\end{aligned}$$

The coordinates of the intersection of the oblate spheroidal cap with the $y = 0$-plane are given by

$$z_P = \alpha b$$

and

$$\begin{aligned}
x_P &= \sqrt{\frac{\alpha b(2\alpha R - \alpha b)}{\alpha^3}} \\
&= \frac{R}{\sqrt{\alpha}}\sqrt{(1 + \cos\theta_c)(1 - \cos\theta_c)} \\
&= \frac{R}{\sqrt{\alpha}}\sin\theta_c,
\end{aligned}$$

with $b = R(1 + \cos\theta_c)$ and $0 < \theta_c < \pi$. The gradient of the oblate spheroid at the point (x_P, z_P) is given by

$$\begin{aligned}
\frac{\alpha^3 x_P}{\alpha R - z_P} &= \frac{\alpha^3\frac{R}{\sqrt{\alpha}}\sin\theta_c}{\alpha R - \alpha R(1 + \cos\theta_c)} \\
&= -\alpha^{\frac{3}{2}}\tan\theta_c.
\end{aligned}$$

The apparent contact angle θ of the oblate spheroid cap is given by

$$\theta = \begin{cases} \arctan\left(\alpha^{\frac{3}{2}}\tan\theta_c\right) & 0 < \theta_c < \frac{\pi}{2}, \\ \frac{\pi}{2} & \theta_c = \frac{\pi}{2}, \\ \arctan\left(\alpha^{\frac{3}{2}}\tan\theta_c\right) + \pi & \frac{\pi}{2} < \theta_c < \pi. \end{cases}$$

APPENDIX E: SURFACE OF THE LIQUID–GAS INTERFACE OF THE PANCAKE SHAPE

The surface area of the liquid–gas interface of the pancake shape consists of a flat circular region at the center, with the area πr_1^2, and the rounded edge, whose surface area S_1 will be derived in the following. The cut-off torus, which represents the rounded edge of

the pancake shape, can be parameterized using spherical coordinates as

$$T(u,v) = \begin{pmatrix} (r_1 + R\sin(v))\cos(u) \\ (r_1 + R\sin(v))\sin(u) \\ R\cos(v) \end{pmatrix}, u \in [0, 2\pi], v \in [0, \theta],$$

and we can calculate the partial derivative as

$$T_u = \begin{pmatrix} -(r_1 + R\sin(v))\sin(u) \\ (r_1 + R\sin(v))\cos(u) \\ 0 \end{pmatrix},$$

$$T_v = \begin{pmatrix} R\cos(v)\cos(u) \\ R\cos(v)\sin(u) \\ -R\sin(v) \end{pmatrix},$$

$$T_u \times T_v = -R(r_1 + R\sin(v)) \begin{pmatrix} \cos(u)\sin(v) \\ \sin(v)\sin(u) \\ \cos(v) \end{pmatrix},$$

$$\|T_u \times T_v\| = R(r_1 + R\sin(v)),$$

and obtain the surface area S_1 as follows:

$$\begin{aligned} S_1 &= \int_{v=0}^{\theta}\int_{u=0}^{2\pi} R(r_1 + R\sin(v))\mathrm{d}u\mathrm{d}v \\ &= 2\pi R[r_1 v - R\cos(v)]_{v=0}^{\theta} \\ &= 2\pi r_1 R\theta + 2\pi R^2(1 - \cos\theta). \end{aligned}$$

Thus, the total surface of the liquid–gas interface is given by

$$S_{LG} = \pi r_1^2 + S_1 = \pi r_1^2 + 2\pi r_1 R\theta + 2\pi R^2(1 - \cos\theta).$$

APPENDIX F: VOLUME OF THE PANCAKE SHAPE

The volume of the pancake can be calculated by splitting it into three parts with the volumes V_1, V_2, and V_3, which are obtained by rotating the colored areas in Fig. 27 around the z-axis. The total volume is then expressed as follows:

$$V = V_1 + V_2 - V_3.$$

The volume V_1 describes an inner cylinder with height $h = R(1 - \cos\theta)$ and base radius r_1. The corresponding formula is given by

$$V_1 = \pi r_1^2 h = \pi r_1^2 R(1 - \cos\theta).$$

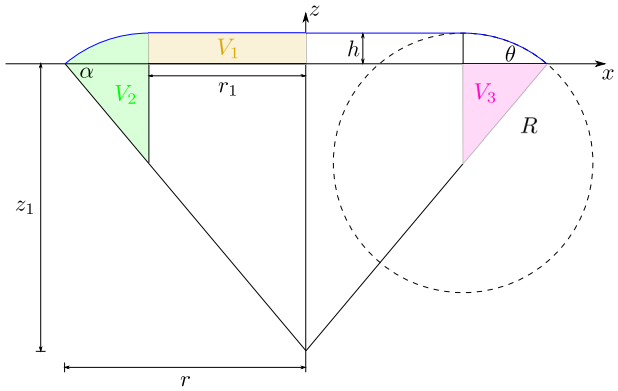

FIG. 27. Schematic cross-sectional view of the droplet formed as a pancake.

The parametrization T of a cut-off torus in spherical coordinates can be used to calculate the volume V_2 as

$$T(a,u,v) = \begin{pmatrix} (r_1 + a\sin(v))\cos(u) \\ (r_1 + a\sin(v))\sin(u) \\ a\cos(v) \end{pmatrix},$$

with $v \in [0,\theta], u \in [0,2\pi], a \in [0,R]$. The Jacobian matrix,

$$J_T = \begin{pmatrix} \sin(v)\cos(u) & -r(a)\sin(u) & a\cos(v)\cos(u) \\ \sin(v)\sin(u) & r(a)\cos(u) & a\cos(v)\sin(u) \\ \cos(v) & 0 & -a\sin(v) \end{pmatrix},$$

with $r(a) = r_1 + a\sin(v)$ and the Jacobian determinant,

$$\det(J_T) = -(r_1 + a\sin(v))a,$$

are required to calculate the volume as

$$\begin{aligned} V_2 &= \int_{u=0}^{2\pi}\int_{v=0}^{\theta}\int_{a=0}^{R} a(r_1 + a\sin(v))\mathrm{d}a\mathrm{d}v\mathrm{d}u \\ &= 2\pi\int_{v=0}^{\theta}\left[\frac{1}{2}a^2 r_1 + \frac{1}{3}a^3\sin(v)\right]_{a=0}^{R}\mathrm{d}v \\ &= 2\pi\int_{v=0}^{\theta}\frac{R^2 r_1}{2} + \frac{R^3}{3}\sin(v)\mathrm{d}v \\ &= \pi R^2 r_1\theta + \frac{2\pi}{3}R^3(1 - \cos\theta). \end{aligned}$$

In conclusion, we will calculate the volume of the third part, which will be subtracted from the second part to ensure the correct

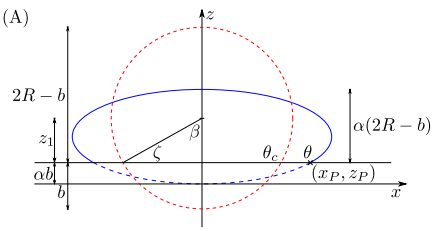

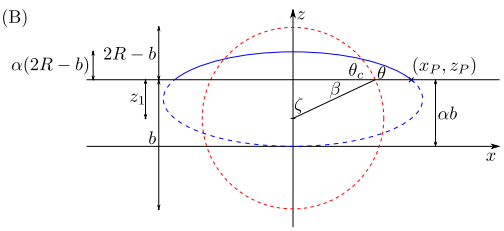

FIG. 26. Schematic side view of the oblate spheroidal cap (blue line) and the imaginary spherical cap (red dashed line) in (a) the hydrophobic case and (b) the hydrophilic case.

calculation of the volume of the pancake, whose base area is flat. The base radius is given by $r = r_1 + R\sin\theta$,

$$z_1 = r\tan\alpha = r\frac{\cos\theta}{\sin\theta}.$$

The third volume V_3 can be considered as a cone cut from the center, with the parametrization $C(\varphi, y)$ in cylindrical coordinates, the Jacobian matrix J_C, and the Jacobian determinant $\det(J_C)$,

$$C(\varphi,y) = \begin{pmatrix} y\cos\varphi \\ y\sin\varphi \\ \tilde{h}\left(1-\frac{y}{r}\right)\end{pmatrix}, \varphi\in[0,2\pi), y\in[r_1,r], \tilde{h}\in[-z_1,0],$$

$$J_C = \begin{pmatrix} -y\sin\varphi & \cos\varphi & 0 \\ y\cos\varphi & \sin\varphi & 0 \\ 0 & -\frac{\tilde{h}}{r} & 1-\frac{y}{r}\end{pmatrix},$$

and

$$\begin{aligned}\det(J_C) &= -y\sin^2\varphi\left(1-\frac{y}{r}\right) - y\cos^2\varphi\left(1-\frac{y}{r}\right)\\ &= -y\left(1-\frac{y}{r}\right).\end{aligned}$$

Thus, the required volume can be calculated as

$$\begin{aligned}V_3 &= \int_{\varphi=0}^{2\pi}\int_{y=r_1}^{r}\int_{\tilde{h}=-z_1}^{0} y\left(1-\frac{y}{r}\right)\mathrm{d}\tilde{h}\mathrm{d}y\mathrm{d}\varphi\\ &= 2\pi z_1\int_{y=r_1}^{r} y-\frac{y^2}{r}\mathrm{d}y\\ &= 2\pi z_1\left(\frac{1}{2}r^2-\frac{r^3}{3r}-\frac{1}{2}r_1^2+\frac{r_1^3}{3r}\right)\\ &= \pi r\frac{\cos\theta}{\sin\theta}\left(\frac{1}{3}r^2-r_1^2+\frac{2r_1^3}{3r}\right),\end{aligned}$$

with $r = r_1 + R\sin\theta$. We have, thus, calculated the volumes of all parts and can now combine them to form the total volume $V = V_1 + V_2 - V_3$, where

$$\begin{aligned}V_1 &= \pi r_1^2 R(1-\cos\theta)\\ V_2 &= \pi R^2 r_1\theta + \frac{2\pi}{3}R^3(1-\cos\theta)\\ V_3 &= \pi r\frac{\cos\theta}{\sin\theta}\left(\frac{1}{3}r^2-r_1^2+\frac{2r_1^3}{3r}\right).\end{aligned}$$

APPENDIX G: HEIGHT OF THE CENTROID OF THE PANCAKE SHAPE

To calculate the height of the centroid, we again use the division into the areas, as in Appendix F for the volume calculation,

$$\begin{aligned}\bar{z} &= \frac{1}{V}\int_V z\mathrm{d}V\\ V\bar{z} &= \int_V z\mathrm{d}V = \int_{V_1} z\mathrm{d}V_1 + \int_{V_2} z\mathrm{d}V_2 - \int_{V_3} z\mathrm{d}V_3.\end{aligned}$$

The cylinder can be parametrized as follows, thus providing the first part for the calculation of $V\bar{z}$ as

$$V_1 = \begin{pmatrix} a\cos\varphi \\ a\sin\varphi \\ z\end{pmatrix}, \varphi\in[0,2\pi), a\in[0,r_1], z\in[0,h],$$

$$J_{V_1} = \begin{pmatrix} -a\sin\varphi & \cos\varphi & 0 \\ a\cos\varphi & \sin\varphi & 0 \\ 0 & 0 & 1\end{pmatrix},$$

$$\begin{aligned}\det(J_{V_1}) &= -a\sin^2\varphi - a\cos^2\varphi = -a,\\ \int_{V_1} z\mathrm{d}V_1 &= \int_{\varphi=0}^{2\pi}\int_{a=0}^{r_1}\int_{z=0}^{h} za\mathrm{d}z\mathrm{d}a\mathrm{d}\varphi\\ &= \frac{\pi}{2}h^2r_1^2\\ &= \frac{\pi}{2}R^2(1-\cos\theta)^2r_1^2.\end{aligned}$$

The second part is calculated as follows:

$$\begin{aligned}\int_{V_2} z\mathrm{d}V_2 &= \int_{u=0}^{2\pi}\int_{v=0}^{\theta}\int_{a=0}^{R}(a\psi - R\xi)a(r_1+a\tau)\mathrm{d}a\mathrm{d}v\mathrm{d}u\\ &= 2\pi\int_{v=0}^{\theta}\int_{a=0}^{R} a^2\psi r_1 - aRr_1\xi + a^3\psi\tau - Ra^2\xi\tau\mathrm{d}a\mathrm{d}v\\ &= 2\pi\int_{v=0}^{\theta}\frac{R^3}{3}\psi r_1 - \frac{R^3}{2}r_1\xi + \frac{R^4}{4}\psi\tau - \frac{R^4}{3}\xi\tau\mathrm{d}v\\ &= 2\pi\left(\frac{R^3r_1}{3}\lambda + \frac{R^4}{8}\lambda^2 + \frac{R^4}{3}\xi^2 - \frac{R^4}{3}\xi - \frac{R^3r_1}{2}\xi\theta\right),\end{aligned}$$

with $\psi = \cos(v)$, $\tau = \sin(v)$, $\xi = \cos\theta$, and $\lambda = \sin\theta$. The third part is determined as

$$\begin{aligned}\int_{V_3} z\mathrm{d}V_3 &= \int_{\varphi=0}^{2\pi}\int_{y=r_1}^{r}\int_{\tilde{h}=-z_1}^{0}\left(\tilde{h}\left(1-\frac{y}{r}\right)\right)y\left(1-\frac{y}{r}\right)\mathrm{d}\tilde{h}\mathrm{d}y\mathrm{d}\varphi\\ &= -\pi z_1^2\int_{y=r_1}^{r} y - 2\frac{y^2}{r} + \frac{y^3}{r^2}\mathrm{d}y\\ &= -\pi z_1^2\left(\frac{r^2}{12} - \frac{r_1^2}{2} + \frac{2r_1^3}{3r} - \frac{r_1^4}{4r^2}\right).\end{aligned}$$

Overall, this leads to the following expression for the height of the centroid, scaled by the volume of the pancake:

$$V\bar{z} = \int_{V_1} z\mathrm{d}V_1 + \int_{V_2} z\mathrm{d}V_2 - \int_{V_3} z\mathrm{d}V_3$$

with

$$\begin{aligned}\int_{V_1} z\mathrm{d}V_1 &= \frac{\pi}{2}R^2(1-\cos\theta)^2r_1^2,\\ \int_{V_2} z\mathrm{d}V_2 &= 2\pi\left(\frac{R^3r_1}{3}\lambda + \frac{R^4}{8}\lambda^2 + \frac{R^4}{3}\xi^2 - \frac{R^4}{3}\xi - \frac{R^3r_1}{2}\xi\theta\right),\\ \int_{V_3} z\mathrm{d}V_3 &= -\pi z_1^2\left(\frac{r^2}{12} - \frac{r_1^2}{2} + \frac{2r_1^3}{3r} - \frac{r_1^4}{4r^2}\right),\end{aligned}$$

with $\xi = \cos\theta$ and $\lambda = \sin\theta$.

REFERENCES

[1] F. Wang, Y. Wu, and B. Nestler, "Wetting effect on patterned substrates," Adv. Mater. **35**(25), 2210745 (2023).

[2] K. Mishra, D. Van den Ende, and F. Mugele, "Recent developments in optofluidic lens technology," Micromachines **7**(6), 102 (2016).

[3] H.-J. Butt, R. Berger, W. Steffen, D. Vollmer, and S. A. L. Weber, "Adaptive wetting—Adaptation in wetting," Langmuir **34**(38), 11292–11304 (2018).

[4] T. Young, "III. An essay on the cohesion of fluids," Philos. Trans. R. Soc. **95**, 65–87 (1805).

[5] E. Bormashenko, "Young, Boruvka–Neumann, Wenzel and Cassie–Baxter equations as the transversality conditions for the variational problem of wetting," Colloids Surf., A **345**(1–3), 163–165 (2009).

[6] E. Bormashenko, "Variational framework for defining contact angles: A general thermodynamic approach," J. Adhes. Sci. Technol. **34**(2), 219–230 (2020).

[7] E. M. Blokhuis, Y. Shilkrot, and B. Widom, "Young's law with gravity," Mol. Phys. **86**(4), 891–899 (1995).

[8] G. Whyman and E. Bormashenko, "Oblate spheroid model for calculation of the shape and contact angles of heavy droplets," J. Colloid Interface Sci. **331**(1), 174–177 (2009).

[9] F. Wang, H. Zhang, and B. Nestler, "Wetting phenomena: Line tension and gravitational effect," Phys. Rev. Lett. **133**, 246201 (2024).

[10] R. Tadmor, "Line energy, line tension and drop size," Surf. Sci. **602**(14), L108–L111 (2008).

[11] F. Aurbach, F. Wang, and B. Nestler, "Wetting phenomena of droplets and gas bubbles: Contact angle hysteresis based on varying liquid–solid and solid–gas interfacial tensions," J. Chem. Phys. **161**(16), 164708 (2024).

[12] V. A. Lubarda and K. A. Talke, "Analysis of the equilibrium droplet shape based on an ellipsoidal droplet model," Langmuir **27**(17), 10705–10713 (2011).

[13] Y. Yu, C. Lv, L. Wang, and P. Li, "The shape of heavy droplets on superhydrophobic surfaces," ACS Omega **5**(41), 26732–26737 (2020).

[14] B. Shapiro, H. Moon, R. L. Garrell, and C.-J. "CJ" Kim, "Equilibrium behavior of sessile drops under surface tension, applied external fields, and material variations," J. Appl. Phys. **93**(9), 5794–5811 (2003).

[15] H. Zhang, Y. Wu, F. Wang, and B. Nestler, "Effect of wall free energy formulation on the wetting phenomenon: Conservative Allen–Cahn model," J. Chem. Phys. **159**(16), 164701 (2023).

[16] R. E. Johnson, Jr., "Conflicts between Gibbsian thermodynamics and recent treatments of interfacial energies in solid-liquid-vapor," J. Phys. Chem. **63**(10), 1655–1658 (1959).

[17] G. W. Gibbs, *Collected Works. Thermodynamics* (Longmans, 1928).

[18] P.-G. de Gennes, F. Brochard-Wyart, and D. Quéré, "Capillarity: Deformable interfaces," in *Capillarity and Wetting Phenomena: Drops, Bubbles, Pearls, Waves* (Springer, 2004), pp. 1–31.

[19] S. Y. Misyura, "Contact angle and droplet evaporation on the smooth and structured wall surface in a wide range of droplet diameters," Appl. Therm. Eng. **113**, 472–480 (2017).

[20] R. Tadmor and P. S. Yadav, "As-placed contact angles for sessile drops," J. Colloid Interface Sci. **317**(1), 241–246 (2008).

[21] E. Yariv, "Shape of sessile drops at small contact angles," J. Fluid Mech. **950**, R4 (2022).

[22] J. Chatterjee, "Limiting conditions for applying the spherical section assumption in contact angle estimation," J. Colloid Interface Sci. **259**(1), 139–147 (2003).

[23] H. Zhang, H. Zhang, F. Wang, and B. Nestler, "Wetting effect induced depletion and adsorption layers: Diffuse interface perspective," ChemPhysChem **25**(14), e202400086 (2024).

[24] L. Jozef Maria Schlangen, *Adsorption and Wetting: Experiments, Thermodynamics and Molecular Aspects* (Wageningen University and Research, 1995).

[25] M. Heier, S. Stephan, F. Diewald, R. Müller, K. Langenbach, and H. Hasse, "Molecular dynamics study of wetting and adsorption of binary mixtures of the Lennard–Jones truncated and shifted fluid on a planar wall," Langmuir **37**(24), 7405–7419 (2021).

[26] F. Wang and B. Nestler, "Wetting and contact-angle hysteresis: Density asymmetry and van der Waals Force," Phys. Rev. Lett. **132**(12), 126202 (2024).

[27] H. Zhang, H. Zhang, F. Wang, and B. Nestler, "Exploration of contact angle hysteresis mechanisms: From microscopic to macroscopic," J. Chem. Phys. **161**(19), 194705 (2024).

[28] H.-J. Butt, J. Liu, K. Koynov, B. Straub, C. Hinduja, I. Roismann, R. Berger, X. Li, D. Vollmer, W. Steffen, and M. Kappl, "Contact angle hysteresis," Curr. Opin. Colloid Interface Sci. **59**, 101574 (2022).

[29] G. Whyman, E. Bormashenko, and T. Stein, "The rigorous derivation of Young, Cassie–Baxter and Wenzel equations and the analysis of the contact angle hysteresis phenomenon," Chem. Phys. Lett. **450**(4–6), 355–359 (2008).